Guidance, navigation and control for the Eddy Brake method.

Natalia Ortiz Gómez[*] and Dr. Scott J.I. Walker [†]

Astronautics Research Group, University of Southampton, SO17 1BJ, United Kingdom

Existing active debris removal methods that require physical contact with the target have applicability limitations depending on the maximum angular momentum that can be absorbed. Therefore, a de-tumbling phase prior to the capturing phase may be necessary. The aim of this article is to study the guidance, navigation and control subsystem of the 'Eddy Brake', an active contactless de-tumbling method based on the generation of eddy currents. The article first presents this method and the main requirements for the control module as well as the necessary sensors for pose estimation on-board the chaser. Furthermore, the linear and rotational dynamics based on the Magnetic Tensor Theory are explained in order to model the chaser-target interactions. In addition, the set of 3D nonlinear dynamical equations that model the de-tumbling process are formulated including a specific control strategy with possible inaccuracies and delays derived from the on-board sensors and actuators. Moreover, a stability analysis is developed in the vicinity of a stable asymptotic state for a simplified 2D configuration where an analytical approach is viable. Finally, two case studies are presented on the Ariane-4 H10 and Ariane-5 EPS upper stages.

---

[*]Stardust ITN Early Stage Researcher, University of Southampton (United Kingdom), N.Ortiz-Gomez@sussed.co.uk.
[†]Associate Professor, University of Southampton (United Kingdom), sjiw@soton.ac.uk.

Nomenclature

$\vec{a}$ = Acceleration vector, $[\text{m·s}^{-2}]$

$\vec{B}$ = Magnetic induction, $[\text{T}]$

d = Distance, $[\text{m}]$

e = Thickness, $[\text{m}]$

$\vec{F}$ = Force, $[\text{N}]$

$\boldsymbol{I_i}$ = Inertia tensor of body i, $[\text{kg·m}^2]$

$\boldsymbol{I}$ = Identity matrix, $[\text{adim}]$

$\boldsymbol{M}, \boldsymbol{M}_{\text{eff}}$ = Magnetic tensor, $[\text{S·m}^4]$

$\vec{m}$ = Magnetic moment, $[\text{A·m}^2]$

m_i = Mass of body i, $[\text{kg}]$

$\vec{r}, \vec{R}, \vec{\rho}$ = Position vector, $[\text{m}]$

$\vec{T}$ = Torque, $[\text{N·m}]$

$\vec{v}$ = Velocity vector, $[\text{m·s}^{-1}]$

χ = Inaccuracy function $[\text{adim}]$

$\vec{\epsilon}_a$ = Relative attitude of the target w.r.t. chaser, $[\text{rad}]$

$\vec{\epsilon}_\theta$ = Relative pointing error of the coil w.r.t. target, $[\text{rad}]$

$\vec{\epsilon}_r$ = Relative distance error between target and chaser, $[\text{adim}]$

$\boldsymbol{\Lambda}$ = Jacobian of magnetic field, $[\text{T·m}^{-1}]$

μ_0 = Vacuum permeability, $[\text{N·A}^{-2}]$

$\mu_\oplus$ = Standard Earth's gravitational parameter, $[\text{km}^3\text{·s}^{-2}]$

μ_{eff} = Efficiency factor, $[\text{adim}]$

$\vec{\omega}, \dot{\vec{\theta}}$ = Angular velocity vector, $[\text{rad·s}^{-1}]$

ϱ = Density, $[\text{kg·m}^{-3}]$

σ = Conductivity, $[\text{S·m}^{-1}]$

τ = Characteristic time, delay $[\text{s}]$

θ = Angle, $[\text{rad}]$

American Institute of Aeronautics and Astronautics

I. Introduction

In the year 2015, two satellite break-ups took place in Low Earth Orbit (LEO), creating new clouds of space debris in one of the most densely populated areas in the near-Earth region [1]. The first event took place on February 2015 when an Air Force weather satellite (DMSP-F13) unexpectedly exploded [2] and the second event happened on November 2015 when a U.S. National Oceanic and Atmospheric Administration satellite (NOAA) suffered a sudden break-up [3]. These types of events are unfortunately becoming more frequent and there is a growing sense within the space science community that there is a tangible threat of the Kessler syndrome becoming a reality. In order to mitigate this problem, new guidelines in the design of space missions have been developed by several national space agencies [4–6]. Within these guidelines, active debris removal (ADR) methods have been proposed as a remediation procedure to remove those objects in orbit that pose the biggest collision risk.

One of the major challenges of the ADR methods that require physical contact with the target (e.g., harpoon, net, robotic arm) is the capture and stabilization of a non-cooperative, rotating object. These methods are only able to capture objects rotating at a maximum angular velocity of a few degrees per second [7–9]. However, optical and radar observations have shown that space debris objects can reach higher rotation rates depending on their orbit, shape and end-of-life conditions [10, 11]. Therefore, a de-tumbling phase prior to the capturing phase may be necessary.

Existing de-tumbling options apply an external torque to the target in order to reduce its angular velocity and this is usually achieved through physical contact with the target object. Among these methods, proposals include applying repeated mechanical impulses with projectiles propelled from a service satellite [12], the use of a brush-type contactor at the tip of the robotic arm [13], the attachment of a propulsive device [14], the attachment of a device that will interact with the Earth's magnetic field [14, 15] and the interaction of a plume engine with the surface of the target [16]. These methods require complex proximity operations and/or highly accurate control in order to achieve a successful deceleration of the angular rates.

Other de-tumbling methods that do not require mechanical contact with the target are based on the generation of electrostatic forces [17]. However, this concept can only be applied to targets located at high altitude orbits, such as geostationary orbits (GEO). This is due to the fact that the plasma Debye length in LEO is low, which does not allow for its application in those regions [18].

The present article focuses on the analysis of the control for an active contactless de-tumbling method based on eddy currents called 'Eddy Brake'. This de-tumbling method is being analyzed and tested in the scope of the phase 0 study of the Agora mission (Active Grabbing & Orbital Removal of Ariane) [19]. Agora is an

American Institute of Aeronautics and Astronautics

ADR mission aimed at removing discarded Ariane rocket bodies (R/Bs). The mission goal is to demonstrate key technologies for ADR processes. These technologies include a contactless de-tumbling system ('Eddy Brake'), a clamping mechanism for capturing and a de-orbit kit placed inside the nozzle of the target by means of a robotic arm.

A de-tumbling method based on the generation of eddy currents was first proposed by Kadaba [20] and some additional research has been carried out since then [21, 22]. The controllability of the magnetic interactions of a two-body system in the context of a de-tumbling process in space is a research area that has not yet been studied and it is of paramount importance in order to prove the feasibility of the 'Eddy Brake' method. A great amount of research has been carried out in the past decade on Electromagnetic Formation Flying Missions (EMFF) in terms of design, dynamics and control [23, 24]. The goal of the EMFF is to generate forces between two or more objects that carry electromagnetic coils on-board and these are usually modeled based on the magnetic dipole approximation. In our case, the main goal is to generate dissipative torques and cancel out the force interactions. Additional missions that are related to the 'Eddy Brake' are those that focus on the generation of eddy currents for space actuation, where the possibility of carrying out a de-tumbling process based on eddy currents has been mentioned [25].

The article is organized as follows. First, Section II describes the physics that drive the Eddy Brake and the systems engineering design envisioned. Then, Section III focuses on the Guidance, Navigation and Control (GNC) subsystem, which is the core of this article. Within this section, the main requirements for this subsystem are first presented (Subsection A) and subsequently, Subsection B is dedicated to the sensors and actuators used in the GNC, focusing on the pose estimation sensors needed for the Eddy Brake.

Section IV focuses on the dynamics of the chaser-target system and the selection of an adequate control strategy. Here, the magnetic interactions between the two objects, employing the Magnetic Tensor Theory (MTT), are first obtained (Subsection A). Moreover, within this Subsection, two different relative configurations of the chaser-target system are analyzed. The first configuration maximizes the magnetic field inside the target and therefore, minimizes the time needed for the de-tumbling process and the second configuration cancels out the relative forces between the chaser and the target.

Within Section IV, the generic 3D dynamical equations for both objects are obtained in Subsection B and then, Subsection C presents the selected control parameters and control strategy. The control is based on a proportional-derivative (PD) controller in which some calibration parameters, referred to as characteristic times for the maneuvers, are included and an optimization criterion to select these parameters is described. In addition, Sub-subsection 1 derives again the 3D dynamical equations for the problem including the proposed control strategy as well as possible inaccuracies and delays derived from sensors and actuators on-board the

chaser. Furthermore, a stability analysis is carried out for a 2D simplified configuration between the two objects in Subsection D. In this study the dynamical equations are linearized to better understand the local stability around the equilibrium position and the effect of the parameters involved.

Finally two case studies are presented in Section V for the 3D dynamical problem including inaccuracies and delays in order to demonstrate the validity of the selected control strategy.

II.   Eddy Brake

'Eddy Brake' is an active, contactless, de-tumbling method based on the generation of eddy currents on a rotating metallic object, subject to a magnetic field. Most man-made objects in orbit contain a high ratio of conductive materials (e.g., aluminum, titanium) that make it possible to induce eddy currents [26]. Suitable target objects for this de-tumbling process include rocket bodies, which contain large, aluminum metallic tanks. Rocket bodies are also high-priority targets for ADR [27].

The de-tumbling process is carried out actively by the chaser, which has a magnetic coil on-board. The de-tumbling system would be positioned several meters away from the target. High temperature superconducting (HTS) wires are used for this purpose. The sizing of the coil is driven by the maximum fairing diameter of the launcher employed [22]. The baseline design of the coil considered throughout this article consists of a coil with a 1.65 meter radius, 500 turns of wire, an electrical intensity of 115 Amperes and a working temperature of 65 K. This is the selected design for the Agora phase 0 study [19].

The Eddy Brake has several advantages with respect to the aforementioned de-tumbling methods:

- Contactless: This method is based on Joule's effect, which is a dissipative effect that gradually decreases the kinetic energy of the object without any mechanical contact. All the problems associated with methods that require the attachment of a device or a grabbing phase are averted.

- Non-invasive: This method is non-invasive for the target object as no mechanical contact is needed. Therefore, the risk of generating new debris during the de-tumbling process is low.

- Control of the target's rotation: The technology considered employs an active method carried out by the chaser. By regulating the relative pointing of the coil with respect to the target, the three components of the target's angular velocity vector can be damped. Moreover, the torques induced on the target are always dissipative. Therefore, there is no risk of increasing the angular velocity of the target. This makes the control of the de-tumbling rate easier compared to those methods that require forces to be exerted at certain points of the target in order to generate torques.

The two most relevant chaser subsystems to support the operation of the Eddy Brake are the thermal

American Institute of Aeronautics and Astronautics

subsystem and the Guidance, Navigation and Control (GNC) subsystem. The thermal subsystem has to guarantee that the coil will always work below its critical temperature and, for this purpose, a loop heat pipe plus a cryocooler or a dewar based system could be employed [19, 28]. The GNC subsystem, which is the primary focus of this article, has to ensure an adequate constant relative pointing of the coil and relative distance between the chaser and the target.

III. GNC subsystem

A. GNC main requirements

The main function of the GNC subsystem is to ensure an adequate chaser-target configuration for the de-tumbling process to be effective. The two main requirements for this subsystem are:

- Adequate relative pointing of the coil. There are two relevant practical configurations, referred to as ($\parallel$) and ($\perp$) and these are further analyzed in Subsection A (Sub-subsection 1). The first one, ($\parallel$), consists in pointing the coil towards the target object, that is, the magnetic moment of the coil should be parallel to the relative position vector between the coil and the COG of the target. In this case the magnetic field created inside the target is maximum and therefore, the de-tumbling time is minimum. The second interesting configuration, ($\perp$), consists in pointing the coil perpendicularly towards the target object, that is, the magnetic moment of the coil should be perpendicular to the relative position vector between the coil and COG of the target. This configuration can cancel out the magnetic forces between the two objects if some constraints with respect to the angular velocity and induced magnetic moment of the target are met.

- Adequate relative distance between the chaser and the target. The magnetic field decays very quickly with the distance. Therefore, the de-tumbling process increases in efficiency as the distance between the chaser and target decreases. Figure 1 indicates the characteristic time of decay of the de-tumbling process for a spherical shell filled in with different percentages of non-conductive material and for different relative distances, using the baseline coil described in Section II. The characteristic time is the time needed to decrease the angular velocity to approximately a third of its initial value [22]. The baseline relative distance needs to be selected based on the maximum allowable risk of collision between the two objects and Figure 1 shows the importance of the relative distance and amount of conductive material on the braking time. As a reference number, the baseline distance selected for the Agora mission is 10 meters between the coil and the COG of the target.

The characteristic time of decay τ of a metallic spherical shell filled in with non-conductive material is equal to [29],

$$\tau = \frac{4\varrho_c}{\sigma_c B^2}(1 + \frac{3}{5}\frac{m_{nc}}{m_c}), \tag{1}$$

where ϱ_c and σ_c are the density and conductivity of the conductive material, m_c and m_{nc} and the masses of the conductive and non-conductive parts and B is the magnetic field.
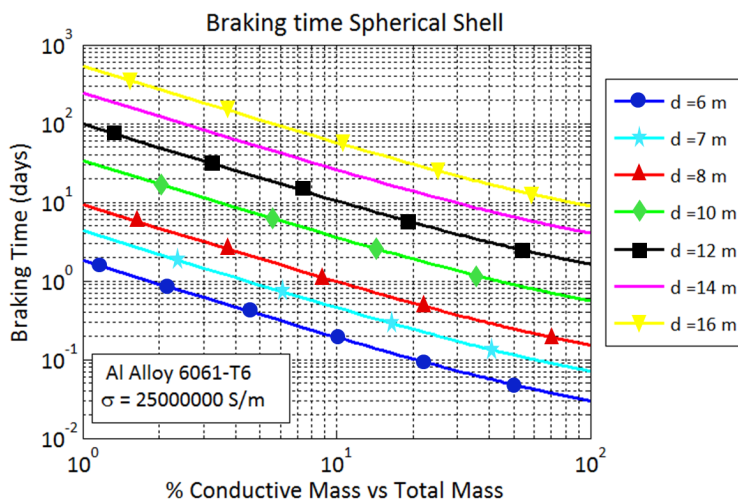

Figure 1: Characteristic time of decay for a spherical metallic shell filled in with different percentages of conductive materials and various distances from the coil.

B.   Target's pose measurement

The de-tumbling process requires the measurement of the relative position and attitude of the target object. There are two possibilities to infer the pose of the target. It can be measured directly by sensors on-board the chaser or it can be obtained indirectly from the magnetic interactions induced on the chaser as a result of the eddy currents generated on the target. This latter option may be very challenging due to the fact that the magnetic forces and torques on the chaser are expected to be of the order of millinewtons and millinewtons per meter (see Section V). These small effects will be covered up by other perturbations that appear on the chaser and therefore, it would be difficult to discriminate each effect. For these reasons, the chaser should carry pose estimation sensors to derive the state of the target.

Pose estimation for active debris removal missions entails various difficulties due to the fact that the target is non-cooperative (e.g. no supportive markers on the surface) and that the physical state of the object may be unknown or uncertain (e.g. fuel left on-board, possible deterioration of the target, etc.).

American Institute of Aeronautics and Astronautics

Current pose estimation sensors for proximity operations can be divided into two major groups; passive camera-based sensors or active light detection and ranging (LIDARs) [30, 31]. Passive sensors may work in the visible range or infrared range and they have lower hardware complexity than active sensors, they are cheaper and their mass and power consumption is lower [32, 33]. However, their resolution is usually poorer than the one of active sensors. Furthermore, visible passive cameras are very sensitive to illumination conditions and they can not be used during eclipse.

Active sensors such as the LIDARs illuminate actively the target with a laser and measure the reflected signal. They are robust sensors with respect to the illumination conditions and they usually have a better resolution than the one provided by passive sensors [32]. However, it should be noted that both active and passive sensors experience problems in the detection of very reflective materials (e.g. MLI) in the short range and low-reflective materials in the long range [34].

Moreover, LIDARs can be scanning LIDARs which sweep the scene with a narrow laser beam, array LIDAR systems (e.g. flash LIDAR) that illuminate the entire scene at once or a combination of both [35, 36]. One of the advantages of the flash LIDAR is that it has no moving components which reduces the risk of failure of the sensor. The scanning LIDAR is usually more effective in the longer range as smaller field of views (FOVs) are needed and therefore, less energy to illuminate the target. As the chaser approaches the target, the scanning LIDAR becomes less efficient because it needs to scan larger FOVs at a faster frame rate. The main disadvantage of the flash LIDAR is that it consumes more power than the scanning LIDAR for the same performance [36].

The pose estimation sensors used for the Eddy Brake should cope with the following requirements:

- Sensor range: The pose estimation sensor should be able to cope with a relative distance in the order of meters for the de-tumbling phase (baseline distance is 10 meters) and the range accuracy should be of the order of centimeters or less.

- FOV: Typical objects targeted for ADR are big size objects (e.g. upper stages) that may be several meters in diameter. The algorithms used for tracking the pose of the target are more accurate if the full target is detected within the FOV of the sensor. Therefore, the selected sensor should have a big FOV in the order of tens of degrees.

- Robustness with respect to any illumination conditions: The magnetic field generated by the chaser should be perpendicular to the angular velocity of the target in order to maximize the induced eddy currents [22]. In addition, the chaser spacecraft may need to acquire different relative configurations in order to damp all the components of the angular velocity of the target object. The necessary relative position of the chaser and target object may not be optimum in terms of illumination conditions

(geometry Sun-target-chaser) and operations during eclipse may be necessary.

- Low exposure time and suitability for rapid ranging scenes: The target's angular velocity may be quite high (> 10 deg/sec) and therefore, the exposure time of the sensor should be low.

- Minimal computational time: The time needed to process the data should be minimal to avoid any delays in the control algorithm as they may affect the stability of the GNC control loop system.

For a relative distance of several meters, the most accurate sensors to measure the pose are the scanning and flash LIDARs. Furthermore, these sensors are less affected by the illumination conditions with respect to optical instruments. The flash LIDAR has some advantages with respect to the scanning LIDAR which makes it a more adequate instrument for the 'Eddy brake'. The flash LIDAR illuminates and gets the data of the scene at once, achieving a high rate of frames per second, while the scanning LIDAR needs to scan the scene. Therefore, this makes scanning LIDARs less suitable for rapid ranging scenes such as a high rate spinning object. Moreover, the flash LIDAR has no moving parts which makes the sensor more reliable. All in all, a flash LIDAR is recommended here as the most adequate pose estimation sensor for the Eddy Brake.

C. Inaccuracies and delays

The sensors and actuators employed in the GNC loop will introduce inaccuracies and delays in the control which may affect the stability of the system [37]. These effects can derive from,

- Sensors on-board the chaser including those sensors that measure its inertial position (e.g. Inertial measurement units (IMUs), star trackers) and pose estimation sensors that measure the relative pose of the target with respect to the chaser.

- Actuators on-board the chaser

- Communications with ground. In this article, it will be assumed that the GNC subsystem is fully autonomous and therefore, this last source of possible error is disregarded.

Typical accuracies achieved during in-orbit tests with passive camera sensors lie in the range of a few centimeters for the relative distance and a few degrees for the relative attitude [31, 33]. Additional sensors such as the TRIDAR have been tested on-board the Space Shuttle for automatic acquisition of the ISS and real-time tracking [34]. The TRIDAR sensor combines a laser based three-dimensional sensor with a thermal imager. The pose accuracies achieved are on the order of 1 cm/1 degree in real time (5 Hz) for final capture operations (< 10 meters). Additional passive and active sensors tested in space for pose estimation are listed in Table 1 including their performance parameters provided by the corresponding manufacturer.

American Institute of Aeronautics and Astronautics

Sensor	Manufacturer	FOV	Range	Accuracy	Nominal Rate
AVGS	NASA	8 deg	$1-300$ m	0.15m/0.5deg (at 10m)	5 Hz
DragonEye 3D Flash LIDAR	ASC	45 deg	< 1.5 km	15cm (3σ)	5 Hz
TRIDAR	Neptec	30 deg	0.5m-2km	1cm/1deg (<10m)	$5-10$ Hz
VNS Flash LIDAR	Ball Aerospace	20 deg	< 5 km	10-20cm $(3\sigma$ at 10m)	< 30 Hz

Table 1: Performance of pose estimation sensors tested in space.

Additional inaccuracies may arise from the actuators employed to execute the maneuvers. For instance, the accuracies achieved by thrusters depend on its minimum impulse bit. This parameter quantifies the minimum thrust that can be commanded by the satellite and the lower the specific impulse of the propellant subsystem, the lower the impulse bit [38]. Hence, a possible way to increase the accuracy of thrusters is to decrease the magnitude of the force. Additional thrust direction errors can be caused by errors in the measurements of inertial attitude sensors or geometric misalignments of the thrusters.

With respect to the possible sources of delays, there is the computational time needed to process the data from pose estimation sensors, the computation of the control maneuvers and their execution. The computational time for the data processing and the control law is usually very low, in the order of milliseconds [33]. Time delays in thrust actuators are due to electrical and mechanical delays in the valve circuits and due to the time needed for the propellant to flow from the valves to the thrusters [39]. Typical values for these delays are in the range of few milliseconds to a few hundreds of milliseconds. For example, a total delay of $\tau = 25$ msec has been estimated for a bi-propellant 10 N thruster [38].

Typical global delays, including the sensors, actuators and communication delays, considered in the analysis of GNC close-loops for spacecraft lie in the order of 1-10 seconds [37, 40].

IV.   Dynamical equations and control strategy

A.   Magnetic interactions

The magnetic interaction between the chaser and the target is analyzed using the Magnetic Tensor Theory (MTT) [22]. A metallic object, hereinafter referred to as the target, when subjected to an external time-varying magnetic field will generate eddy current loops (also called Foucault currents) in its metallic components due to Faraday's law of induction [41]. These electric current loops can be created inside a sta-

tionary conductor subject to a time-varying magnetic field or a moving object (linear or rotational motion) subject to a constant magnetic field. The magnetic moment $\vec{m}$ for a generic body can be expressed as shown in Equation (2),

$$\vec{m} = \boldsymbol{M}\vec{\Omega}, \tag{2}$$

where $\boldsymbol{M}$ is the Magnetic tensor of the object and $\vec{\Omega}$ is a vector that indicates the source of generation of the eddy currents [22]. The Magnetic Tensor is a 3×3 constant tensor intrinsic to each body that describes the body's conductive mass distribution. In this problem, we are interested in generating eddy currents due to the fact that the target object has a relative angular velocity $\vec{\omega}$ with respect to an external constant magnetic field $\vec{B}$. Under these circumstances, the magnetic moment acquires the form,

$$\vec{m} = \boldsymbol{M}(\vec{\omega} \times \vec{B}). \tag{3}$$

Moreover, the cross product of the magnetic moment of the rotating object and the external magnetic field will induce a torque on the target which has the form,

$$\vec{T} = \vec{m} \times \vec{B} = (\boldsymbol{M}(\vec{\omega} \times \vec{B})) \times \vec{B}. \tag{4}$$

The torque shown in Equation (4) is a dissipative torque that decreases the angular velocity of metallic object. The subsequent reduction of the kinetic energy of the target is related with the fact that this energy is dissipated into heat, generated by the eddy current loops (Joule's law). Note that if the external magnetic field $\vec{B}$ is parallel to the angular velocity vector of the target $\vec{\omega}$, no torque is created. This means that the coil's magnetic moment needs to make a non-zero angle with respect to $\vec{\omega}$ in order to generate the desired dissipative torque.

Furthermore, the magnetic field created by the coil on-board the chaser spacecraft is a non-uniform field inside the target object. This results in the appearance of a net force at the target's COG and reduction in the efficiency of the de-tumbling torque [43]. This loss in efficiency can be approximately quantified by an efficiency factor μ_{eff} that multiplies the Magnetic tensor, resulting in an effective Magnetic tensor [22],

$$\boldsymbol{M}_{\text{eff}} = \mu_{\text{eff}} \cdot \boldsymbol{M}. \tag{5}$$

Hereinafter, the target will be denoted by the sub-index t and the chaser by the sub-index c. The induced torque $\vec{T}_{ct}$ and induced force $\vec{F}_{ct}$ on the target by the chaser are given by Equations (6) and (7) [22],

$$\vec{T}_{ct} = (\boldsymbol{M}_{\text{eff}}(\vec{\omega} \times \vec{B}_{Gt})) \times \vec{B}_{Gt}, \tag{6}$$

$$\vec{F}_{ct} = \boldsymbol{\Lambda_{Gt}} \boldsymbol{M}_{\text{eff}}(\vec{\omega} \times \vec{B}_{Gt}), \tag{7}$$

where $\boldsymbol{M}_{\text{eff}}$ is the effective magnetic tensor, $\vec{\omega}$ is the relative angular velocity of the target with respect to the chaser, $\vec{B}_{Gt}$ is the magnetic field at the center of gravity (COG) of the target (denoted by the subscript Gt) and $\boldsymbol{\Lambda_{Gt}}$ is the Jacobian tensor of the magnetic field at the COG of the target.

So far, the magnetic forces and torques that appear on the target have been analyzed. Taking into account the conservation of momentum of the chaser-target system [22], a force of equal magnitude and opposite direction will be generated on the chaser $\vec{F}_{tc}$,

$$\vec{F}_{tc} = -\vec{F}_{ct}. \tag{8}$$

Furthermore, by computing the resultant torques acting on the chaser-target system, the torque that acts on the chaser $\vec{T}_{tc}$ can be derived [22],

$$\vec{T}_{tc} + \vec{T}_{ct} + (\vec{r} \times \vec{F}_{ct}) = \vec{0} \rightarrow \vec{T}_{tc} = -\vec{T}_{ct} - (\vec{r} \times \vec{F}_{ct}) \tag{9}$$

where $\vec{r}$ is the position vector of the COG of the target with respect to the COG of the chaser. Figure 2 depicts the chaser-target interactions for a spherical shell target.
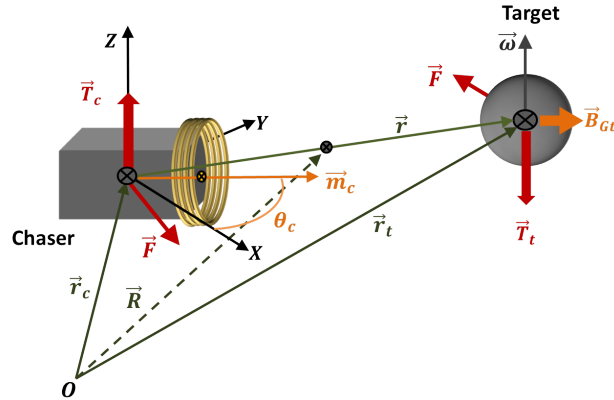

Figure 2: Chaser-target interactions.

1. Relative configurations chaser-target

Two limiting extreme configurations of the coil with respect to the target for the de-tumbling process are presented in this section (i.e. all other pointing configurations can be expressed as a combination of the two cases described here). The first one, named as ($\parallel$), consists in pointing the coil towards the COG of the target object, that is, the magnetic moment of the coil should be parallel to the relative position vector

between the coil and the COG of the target. In this case the magnetic field created inside the target is maximum and therefore, the de-tumbling time is minimum.

The second interesting configuration, named as ($\perp$), consists in pointing the coil perpendicularly towards the target object, that is, the magnetic moment of the coil should be perpendicular to the relative position vector between the coil and the COG of the target. This configuration can minimize or cancel out the magnetic forces between the two objects if some constraints are met. However, the magnetic field decreases to half of the value with respect to configuration ($\parallel$) and the characteristic time of the de-tumbling process is divided by four, which makes the de-tumbling process more time-consuming.

In this section, an analytical development based on magnetic dipoles is used to identify the geometries which result in no magnetic forces appearing during the de-tumbling process. The magnetic dipole approximation is only valid if the relative distance between the two objects is big compared with the size of the objects. For the active de-tumbling process, the size of the coil, the target object and their relative distance may be of the same order of magnitude and therefore, this approximation will be less accurate than the MTT. However, it avoids the need to compute the Jacobian tensor of the magnetic field and it may be used as a first assessment of the force (See Annex VI). The force between two magnetic dipoles is given by [42],

$$\vec{F} = \frac{3\mu_0}{4\pi r^5}((\vec{m}_t \cdot \vec{r})\vec{m}_c + (\vec{m}_c \cdot \vec{r})\vec{m}_t + (\vec{m}_c \cdot \vec{m}_t)\vec{r} - \frac{5(\vec{m}_t \cdot \vec{r})(\vec{m}_c \cdot \vec{r})}{r^2}\vec{r}), \tag{10}$$

where $\vec{m}_t$ and $\vec{m}_c$ are the magnetic dipoles of the target and the chaser and $\vec{r}$ is the relative state vector between the two objects.

Consequently, in order to have no forces between the two objects, the following conditions must be met,

- The magnetic moment of the coil must be perpendicular to $\vec{r}$ ($\vec{m}_c \perp \vec{r}$).

- The magnetic moment of the target must be perpendicular to $\vec{r}$ ($\vec{m}_t \perp \vec{r}$).

- The magnetic moment of the target and the chaser must be perpendicular to each other ($\vec{m}_t \perp \vec{m}_c$).

The previous conditions apply to any type of object. In the case of a spherical shell, the relative configuration that cancels out the magnetic forces can be easily identified as follows. The magnetic moment of a spherical target is given by,

$$\vec{m}_t = \boldsymbol{M}\vec{\Omega} = \frac{2\pi}{3}\sigma R^4 e(\vec{\omega} \times \vec{B}) \tag{11}$$

and the force will be zero when the configuration depicted in Figure 3 takes place.
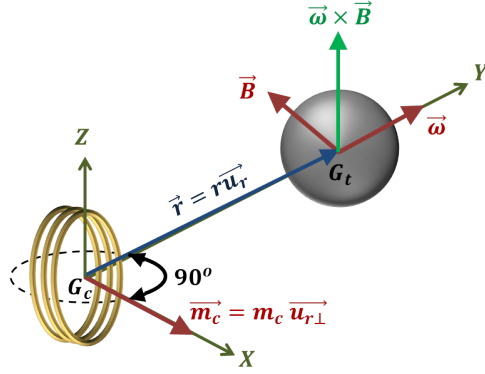
American Institute of Aeronautics and Astronautics

Figure 3: Configuration of null force on a spherical shell.

A priori, configuration ($\perp$) may seem interesting in pursuing a reduction of the fuel consumption due to the fact that no magnetic forces, that would separate both bodies, take place. However, this configuration depends on the directions of the angular velocity and magnetic moment of the target, which may also be uncertain. In addition, the magnetic tensor of the target may be a time-varying tensor due to the rotation of the body fixed frame of the target with respect to an Earth Centered Inertial (ECI) reference frame. Hence, configuration ($\perp$) may require complex operations for a longer period of time that would increase the total ΔV instead of reducing it. The configuration ($\perp$) would only be of interest if the angular velocity of the target and its physical properties would be such that the chaser could be positioned at the same orbit as the target in order to avoid costly maneuvers due to differences in the orbital velocities of the two objects.

Therefore, configuration ($\parallel$) seems more realistic from the operational point of view as it will reduce the operational times of the de-tumbling process and it gives more freedom in the choice of the formation flying configurations.

B. 3D Dynamical equations

The full 3D dynamical problem is described by a set of non-linear differential equations listed in (12, 13, 14, 15) which involve the position and attitude of the chaser and the target. Equations (12, 13) indicate the motion of the COG of each object and they are expressed in the ECI reference frame. Equations (14, 15) are Euler's equations which indicate the angular evolution for each object and it should be noted that these equations are expressed in the body reference frames of each object [44]. The body reference frame is a fixed reference frame to a certain body with its origin at the COG of the object.

$$m_t \ddot{\vec{r}}_t = \vec{F}_{ct} + \sum_i \vec{F}_{ext_i,t}, \tag{12}$$

$$m_c \ddot{\vec{r}}_c = \vec{F}_{tc} + \sum_i \vec{F}_{ext_i,c} + \sum_i \vec{F}_{mi,c}, \tag{13}$$

$$\boldsymbol{I_t} \dot{\vec{\omega}}_t + \vec{\omega}_t \times \boldsymbol{I_t} \vec{\omega}_t = \vec{T}_{ct} + \sum_i \vec{T}_{ext_i,t}, \tag{14}$$

$$\boldsymbol{I_c} \dot{\vec{\omega}}_c + \vec{\omega}_c \times \boldsymbol{I_c} \vec{\omega}_c = \vec{T}_{tc} + \sum_i \vec{T}_{ext_i,c} + \sum_i \vec{T}_{mi,c}, \tag{15}$$

where m_i is the mass of the studied body $(i = t, c)$, $\boldsymbol{I_i}$ is the inertia tensor, $\vec{r}_i$ is the inertial position in the ECI reference frame, $\vec{\omega}_i$ is the angular velocity vector of the body reference frame with respect to the ECI reference frame, expressed in the body reference frame. Moreover, the sum of forces $\sum_i \vec{F}_{ext_i}$ and torques $\sum_i \vec{T}_{ext_i}$ are the external environmental perturbations that may affect each body and the forces and torques named as $\sum_i \vec{F}_{mi,c}$ and $\sum_i \vec{T}_{mi,c}$ are the maneuvers executed by the chaser.

In Subsection VI of the Annex, Equations (12, 13, 14, 15) are transformed in the usual way for their numerical integration by adding function derivatives which results in a system of first order differential equations. This numerical integration process is used to solve the numerical simulations in Sections IV.D and V.

The following mathematical developments within Section IV are oriented towards an approximate analytical study of the problem for qualitative purposes. To this end, the following variables are defined for their further use throughout the paper. First of all, the relative position $\vec{r}$ of the target with respect to the chaser and its unitary vector $\vec{u}_r$ are computed in Equation (16),

$$\vec{r} = \vec{r}_t - \vec{r}_c, \quad \vec{u}_r = \frac{\vec{r}}{|\vec{r}|}. \tag{16}$$

In addition, the relative angular velocity of the target with respect to the chaser is denoted by the variable and $\dot{\vec{\epsilon}}_a$, shown in Equation (17).

$$\dot{\vec{\epsilon}}_a = \vec{\omega}_t - \vec{\omega}_c. \tag{17}$$

1.   Earth modeled as a point mass and magnetic interactions

Within this section, the relative motion between the chaser and the target is analyzed considering the gravity of the Earth modeled as a point mass, the magnetic interactions between the two objects and the orbital maneuvers executed by the chaser. These equations will be later used for the stability analysis in Subsection D.

It should be noted that it has been decided not to employ classical solutions for the relative motion, such as the Clohessy-Wiltshire equations [30] but it has been decided to derive the equations from the basic Newton's Second Law of motion in an inertial reference frame. The classical Clohessy-Wiltshire equations are typically

expressed in the rotating target local orbital frame and the inclusion of the magnetic interactions in these equations is not straightforward. Under these conditions, the general equations specified in Subsection B are simplified,

$$m_t \ddot{\vec{r}}_t = \vec{F}_{ct} + \vec{F}_{gt}, \tag{18}$$

$$m_c \ddot{\vec{r}}_c = -\vec{F}_{ct} + \vec{F}_{gc} + \sum_i \vec{F}_{mi,c}, \tag{19}$$

$$\boldsymbol{I_t}\dot{\vec{\omega}}_t + \vec{\omega}_t \times \boldsymbol{I_t}\vec{\omega}_t = \vec{T}_{ct}, \tag{20}$$

$$\boldsymbol{I_c}\dot{\vec{\omega}}_c + \vec{\omega}_c \times \boldsymbol{I_c}\vec{\omega}_c = \vec{T}_{tc} + \sum_i \vec{T}_{mi,c}, \tag{21}$$

where $\vec{F}_{gi}$ $(i = (t,c))$ is the gravitational force at the COG of each object given by,

$$\vec{F}_{gi} = -\mu_\oplus \frac{m_i \vec{r}_i}{r_i^3}, \quad i = (t,c) \tag{22}$$

and $\mu_\oplus = 398600.44$ km^{3}s^{-2} is the standard Earth's gravitational parameter. Moreover, the COG of the chaser-target system is described by the inertial state vector $\vec{R}$,

$$m\vec{R} = m_t \vec{r}_t + m_c \vec{r}_c, \quad m = m_t + m_c \tag{23}$$

and the position vectors $\vec{r}_i$ $(i = t,c)$ may also be expressed as,

$$\vec{r}_t = \vec{R} + \frac{m_c}{m}\vec{r} = \vec{R} + \vec{\rho}_t, \tag{24}$$

$$\vec{r}_c = \vec{R} - \frac{m_t}{m}\vec{r} = \vec{R} + \vec{\rho}_c. \tag{25}$$

where $\vec{\rho}_i$ $(i = t,c)$ are position vectors of the target and chaser w.r.t. the COG of the system and it holds that $|\vec{\rho}_i| << \left|\vec{R}\right|$. By expanding $\frac{\vec{r}_i}{r_i^3}$ in a Taylor series with respect to variable $\vec{\rho}_i$ up to the first linear term, the following expression is obtained for $\vec{F}_{gi}$,

$$\frac{\vec{r}_i}{r_i^3} \approx \frac{\vec{R}}{R^3} + \boldsymbol{P}\frac{\vec{\rho}_i}{R^3} \rightarrow \vec{F}_{gi} \approx -\mu_\oplus m_i (\frac{\vec{R}}{R^3} + \boldsymbol{P}\frac{\vec{\rho}_i}{R^3}), \tag{26}$$

where the matrix $\boldsymbol{P}$ is equal to [30],

$$\boldsymbol{P} = \boldsymbol{I} - 3\vec{u}_R\vec{u}_R^T, \quad \vec{u}_R = \frac{\vec{R}}{R}. \tag{27}$$

The motion of the COG of the system can be decoupled from the interaction between the chaser and the

American Institute of Aeronautics and Astronautics

target, assuming that the gravity force at the COG of the system, $\vec{F}_g$, dominates over the maneuvering forces exerted by the chaser,

$$m\ddot{\vec{R}} = m_t\ddot{\vec{r}}_t + m_c\ddot{\vec{r}}_c = \vec{F}_g + \sum \vec{F}_{mc} \approx \vec{F}_g \tag{28}$$

and $\vec{F}_g$ is equal to,

$$\vec{F}_g = \vec{F}_{gc} + \vec{F}_{gt} \approx -\mu_\oplus m_c \left(\frac{\vec{R}}{R^3} - \frac{m_t}{mR^3}\boldsymbol{P}\vec{r} \right) - \mu_\oplus m_t \left(\frac{\vec{R}}{R^3} + \frac{m_c}{mR^3}\boldsymbol{P}\vec{r} \right) = -\mu_\oplus \frac{m}{R^3}\vec{R}. \tag{29}$$

Therefore, the differential equation describing the motion of the COG of the system is decoupled from the magnetic interactions between the chaser and target objects and it reduces to Equation (30). This result just reflects a virtual object of mass $m = m_t + m_c$ orbiting around the Earth. Although the mathematical process from Equation (18) until (30) refers to basic space flight dynamics [30], a self-contained development has been included in order to clarify the notation employed and the hypothesis made to reach Equation (30). These hypothesis are primarily two: first, the cancellation of the magnetic interactions as a consequence of the conservation of linear momentum of the hypothetically isolated chaser-target system; and second, the dominance of the gravity forces with respect to the chaser's maneuvers, which are assumed to be small.

$$\ddot{\vec{R}} \approx -\frac{\mu_\oplus}{R^3}\vec{R}. \tag{30}$$

Furthermore, an additional differential equation is needed to describe the relative position of the target w.r.t. the chaser. The position vector of the target with respect to the chaser verifies,

$$\ddot{\vec{r}} = \ddot{\vec{r}}_t - \ddot{\vec{r}}_c = \frac{\vec{F}_{ct}}{m_{red}} - \frac{1}{m_c}\sum \vec{F}_{mc} + \vec{a}_{gr}, \tag{31}$$

where the reduced mass is $m_{red} = \frac{m_t m_c}{m_t + m_c}$ and the acceleration caused by the Earth's gravity $\vec{a}_{gr}$ is equal to,

$$\vec{a}_{gr} = -\mu_\oplus \frac{\vec{r}_t}{r_t^3} + \mu_\oplus \frac{\vec{r}_c}{r_c^3} \approx -\frac{\mu_\oplus}{R^3}\boldsymbol{P}\vec{r}. \tag{32}$$

Therefore, the set of 3D dynamical equations for this specific problem is,

$$\ddot{\vec{R}} \approx -\frac{\mu_\oplus}{R^3}\vec{R},$$
$$\ddot{\vec{r}} = \frac{\vec{F}_{ct}}{m_{red}} - \frac{\mu_\oplus}{R^3}\boldsymbol{P}\vec{r} - \frac{1}{m_c}\sum_i \vec{F}_{mi,c},$$
$$\boldsymbol{I_t}\dot{\vec{\omega}}_t + \vec{\omega}_t \times \boldsymbol{I_t}\vec{\omega}_t = \vec{T}_{ct},$$
$$\boldsymbol{I_c}\dot{\vec{\omega}}_c + \vec{\omega}_c \times \boldsymbol{I_c}\vec{\omega}_c = \vec{T}_{tc} + \sum_i \vec{T}_{mi,c},$$
$$\tag{33}$$

where the degrees of freedom are the vectors $\vec{R}$, $\vec{r}$, $\vec{\theta}_t$ and $\vec{\theta}_c$.

C. Control maneuvers

In this section, a set of control maneuvers are formulated for the general 3D movement of the two objects. The theoretical stability analysis is developed later in Subsection D for a simplified 2D configuration where an analytical approach is viable. The general 3D strategy is applied in the final case studies (see Section V) in order to test numerically the validity of the proposed maneuvers.

The control variables identified to achieve a stable configuration throughout the de-tumbling process are gathered in vector $\vec{Z}$ defined in the expression (34),

$$\vec{Z} = \begin{bmatrix} \epsilon_r \\ \epsilon_\theta \\ \epsilon_a \\ \omega_c \end{bmatrix}. \tag{34}$$

The variable ϵ_r represents the relative distance error with respect to the desired relative distance d between the two objects

$$\epsilon_r = \frac{|\vec{r}| - d}{d}. \tag{35}$$

Moreover, ϵ_θ represents the error in the relative pointing of the coil. If the desired angle between the magnetic moment of the coil $\vec{m}_c$ and the relative vector $\vec{r}$ is θ_d, a possible way to define ϵ_θ is,

$$\epsilon_\theta = \cos(\theta_d) - \vec{u}_r \cdot \frac{\vec{m}_c}{|\vec{m}_c|}, \tag{36}$$

although other equivalent functions to control the relative pointing may be more convenient depending on each specific problem.

The derivatives $\dot{\epsilon}_r$ and $\dot{\epsilon}_\theta$, which will also be used for the control, may be computed as shown in Equations (37, 38).

$$\dot{\epsilon}_r = \frac{\left|\dot{\vec{r}}\right|}{d}, \tag{37}$$

$$\dot{\epsilon}_\theta = -\left(\vec{\omega}_c \times \frac{\vec{m}_c}{|\vec{m}_c|}\right) \cdot \vec{u}_r - \left(\frac{\dot{\vec{r}}}{|\vec{r}|} - \frac{(\vec{r} \cdot \dot{\vec{r}})}{|\vec{r}|^3}\vec{r}\right) \cdot \frac{\vec{m}_c}{|\vec{m}_c|}. \tag{38}$$

Furthermore, the control vector $\vec{Z}$ contains two additional control variables $\epsilon_a = |\vec{\epsilon}_a|$ (defined in Equation 17) and $\omega_c = |\vec{\omega}_c|$. As described in Subsection B, $\vec{\epsilon}_a$ is the relative attitude of the target with respect to the

chaser. It must be noted that the final goal of the de-tumbling process is to nullify $\dot{\epsilon}_a$, so that the target no longer rotates with respect to the chaser. The last control parameter is the modulus of the inertial angular velocity of the chaser $\vec{\omega}_c$. The inclusion of this last control variable, which may not be as intuitive as the previous ones, is explained subsequently.

Figure 4 depicts the kinematic and control variables of a simplified 2D configuration that helps to visualize the problem. In this simplified version of the 3D full dynamical problem, both bodies are assumed to move in coplanar orbits ((X,Y) plane) and to rotate about an axis perpendicular to the orbit (Z axis). If only the variables ϵ_r, ϵ_θ and ϵ_a are controlled, the configuration shown in the right-hand side of Figure 4 would take place. The angular velocity of the target object would transform into a rotational motion of the two bodies around the COG of the combined two-body system. The chaser spacecraft would increase its inertial angular velocity ω_c until it matches the angular velocity of the target object. When the relative angular velocity between the two objects becomes zero, eddy currents would no longer be induced on the target object and the de-tumbling process would stop. Therefore, the inertial rotation of the chaser needs to be included in the control. The selected control strategy is based on a proportional-derivative (PD) controller. This classical
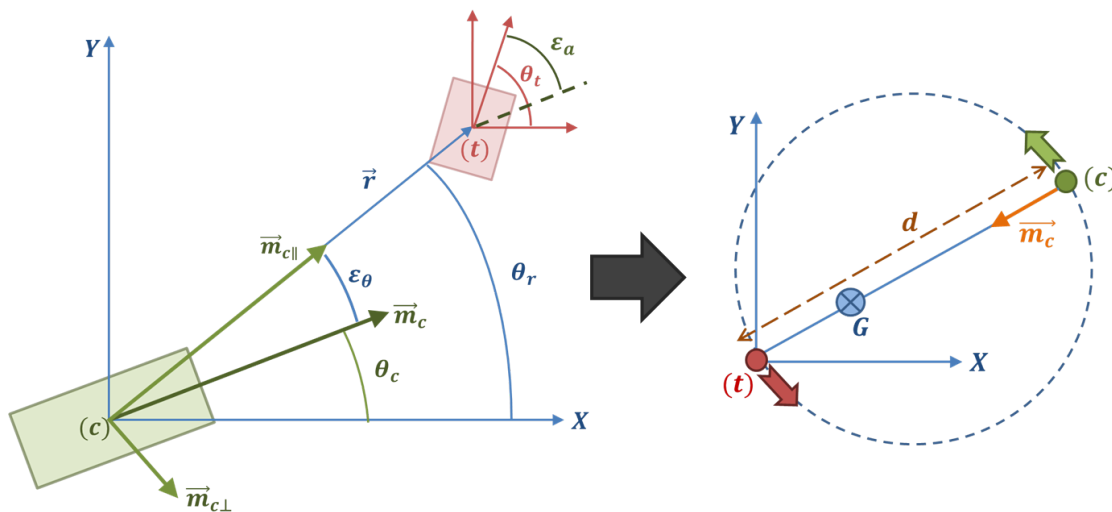

Figure 4: Chaser-target interactions for a simplified 2D configuration (left image) and stable configuration under the control of just ϵ_r and ϵ_θ (right image).

and simple approach is frequently used for the GNC design [30,33]. Equations (39, 40, 41) indicate the maneuvers executed by the chaser which are proportional to the control variables and their derivatives. The parameters τ_{mi} ($i = 1,5$) that appear in the formulas below are some 'characteristic times' of the maneuvers which need to be calibrated in order to achieve a stable and optimal control.

$$\vec{F}_{mc1} = m_c d \left(\frac{\epsilon_r}{\tau_{m1}^2} + \frac{\dot{\epsilon}_r}{\tau_{m2}} \right) \vec{u}_r, \tag{39}$$

$$\vec{F}_{mc2} = \left(\frac{m_c d}{\tau_{m3}}\right)(\vec{\omega}_c \times \vec{u}_r), \tag{40}$$

$$\vec{T}_{mc1} = (\frac{\epsilon_\theta}{\tau_{m4}^2} + \frac{\dot{\epsilon}_\theta}{\tau_{m5}})\boldsymbol{I_c}(\frac{\vec{m}_c}{|\vec{m}_c|} \times \vec{u}_r). \tag{41}$$

As it will be shown in subsequent case studies, an efficient criterion to deduce these characteristic times τ_{mi} is based on the minimization of the total energy consumption, that is, the minimization of the total ΔV of the de-tumbling process. The objective function of the optimization problem is expressed by Equation (42) together with additional possible constraints on the control variables represented by Equations (43),

$$\min(\Delta V) = \min\left(\sum_i \int_0^{t_f} \frac{1}{m_c(t)}\left|\vec{F}_{mc_i}(t)\right|dt + \sum_i \int_0^{t_f} \frac{1}{d_{th}m_c(t)}\left|\vec{T}_{mc_i}(t)\right|dt\right), \tag{42}$$

$$|\epsilon_r| \le c_1, \quad |\epsilon_\theta| \le c_2, \quad |\dot{\epsilon}_a| \le c_3, \quad |\omega_c| \le c_4, \tag{43}$$

where t_f is the final time of the de-tumbling process, d_{th} is the sum of the lever-arm distances of the thrusters on-board the chaser and c_i $(i = 1, 4)$ are the constraints given to each control variable.

1. Inaccuracies and delays formulation

As explained in Subsection C, inaccuracies in the control process may come from measurement inaccuracies of the sensors or errors in the execution of the maneuvers by the actuators. In order to include the possible inaccuracies in the control, the characteristic times of the control maneuvers and the related parameters R_{mi}, ($R_{m1} = \frac{1}{\tau_{m1}^2}$, $R_{m2} = \frac{1}{\tau_{m2}}$, $R_{m3} = \frac{1}{\tau_{m3}}$, $R_{m4} = \frac{1}{\tau_{m4}^2}$, $R_{m5} = \frac{1}{\tau_{m5}}$), are treated as functions of time in the numerical integration process. The following change in the R_{mi} parameters is performed using,

$$R_m = constant \to R_m + \delta R_m(t) = (1 + \chi(t))R_m, \tag{44}$$

where a new function $\chi(t)$ is introduced in order to take into account the inaccuracies derived from sensors and actuators. This is modeled as a stochastic variable with mean null value and root mean square error χ_{cm},

$$\overline{\chi} = 0, \quad \sqrt{\overline{\chi^2}} = \chi_{cm}. \tag{45}$$

The function $\chi(t)$ is generated with a random function RND of uniform probability as,

$$\chi(t) = \sqrt{3}(2 \cdot RND - 1)\chi_{cm}, \tag{46}$$

American Institute of Aeronautics and Astronautics

which complies with the conditions shown in Equation (45). Based on the literature review done in Subsection C, current pose estimation sensors achieve range accuracies in the order of few centimeters or less at our baseline distance of 10 meters, which is approximately a 0.1% error ($\chi_{cm} = 0.001$). Attitude accuracies for pose estimation sensors are in the order of 1 degree or less, which is approximately a 0.3% error ($\chi_{cm} = 0.003$). Additional errors may come from other sensors and the on-board actuators.

The time delays derived from the software and hardware on-board the chaser also need to be included in the control. For this purpose, a certain delay τ is introduced in the maneuvers executed by the chaser spacecraft.

All in all, the generic 3D dynamical equations including all these effects are listed in (47),

$$
\begin{aligned}
m_t\ddot{\vec{r}}_t(t) &= \vec{F}_{ct}(t) + \sum_i \vec{F}_{ext_i,t}(t), \\
m_c\ddot{\vec{r}}_c(t) &= \vec{F}_{tc}(t) + \sum_i \vec{F}_{ext_i,c}(t) + \sum_i (1+\chi_i(t-\tau))\vec{F}_{mi,c}(t-\tau), \\
\boldsymbol{I_t}\dot{\vec{\omega}}_t(t) + \vec{\omega}_t(t) \times \boldsymbol{I_t}\vec{\omega}_t(t) &= \vec{T}_{ct}(t) + \sum_i \vec{T}_{ext_i,t}(t), \\
\boldsymbol{I_c}\dot{\vec{\omega}}_c(t) + \vec{\omega}_c(t) \times \boldsymbol{I_c}\vec{\omega}_c(t) &= \vec{T}_{tc}(t) + \sum_i \vec{T}_{ext_i,c} + \sum_i (1+\chi_i(t-\tau))\vec{T}_{mi,c}(t-\tau).
\end{aligned}
\tag{47}
$$

D. Stability analysis

In this section, a simplified 2D analytical study is carried out to assess the stability of the chaser-target system in the vicinity of the equilibrium state $\vec{Z} = \vec{0}$. The approximate theoretical approach developed in this section has been a useful tool to determine the appropriate kind and number of maneuvers, before dealing with costly and time consuming 3D numerical simulations presented in the following section.

For this purpose, the target and the chaser are assumed to move in coplanar orbits (X, Y plane) and to be able to rotate about an axis perpendicular to the orbital plane (Z axis) (see Figure 4). Furthermore, the perturbations taken into account are the Earth modeled as a point mass and the magnetic interactions between the two objects. In addition, in order to further simplify the problem, the considered target is a spherical shell. These simplifications are necessary to facilitate an analytical study. Therefore, the conclusions derived here are only theoretical and they must be confirmed by numerical simulations as the ones provided in Section V.

Under these assumptions, the number of degrees of freedom is reduced to six,

$$
\vec{R} = R\vec{u}_R = R[\cos\theta_R, \sin\theta_R, 0],
\tag{48}
$$

$$\vec{r} = r\vec{u}_r = r[\cos\theta_r, \sin\theta_r, 0], \tag{49}$$

$$\vec{\theta}_t = [0, 0, \theta_t], \tag{50}$$

$$\vec{\theta}_c = [0, 0, \theta_c], \tag{51}$$

where θ_R is the angle used to locate the COG of the system in the ECI frame, θ_r is the angle used to locate the orientation of the relative position vector with respect to the ECI frame and θ_t and θ_c are the attitude angles of each body of their body-fixed reference frames with respect to the ECI frame.

Moreover, in this 2D problem, the error in the relative pointing ϵ_θ and the relative attitude of the target with respect to the chaser ϵ_a (see Figure 4) may be formulated in a simpler way than the general 3D formulas as expressed in Equations (52) and (53),

$$\epsilon_\theta = \theta_r - \theta_c, \tag{52}$$

$$\epsilon_a = \theta_t - \theta_c. \tag{53}$$

The magnetic interactions between the chaser and the target for the specified 2D problem are derived in Appendix Subsection VI.

Introducing theses magnetic forces and torques, Equations (79,81, 82), together with the chaser maneuvers, Equations (39,40,41) in (33), the 2D dynamical equations are obtained below. Equation (54) describes the translation of the COG of the system, Equation (55) describes the relative translation of the system and Equations (56, 57) describe the evolution of the uniaxial rotation of the target and the chaser respectively. Note that in these last two Euler equations the terms $\vec{\omega}_i \times \mathbf{I}_i\vec{\omega}_i$ $(i =, t, c)$ from the original Euler's equations (14, 15) have vanished. The dropping of the gyroscopic term is also due to the simplification to 1-dimensional rotation. In the case of the target, which is modeled as a spherical shell in this section, all axes are principal axis of inertia, so the disappearance of this term is straightforward. In the case of the chaser, it has been assumed that the Z axis is a principal axis of inertia.

$$\ddot{\vec{R}} \approx -\frac{\mu_\oplus}{R^3}\vec{R}, \tag{54}$$

$$\frac{\ddot{\vec{r}}}{d} = \left(\frac{\dot{\epsilon}_a}{\tau_r(1+\epsilon_r)^7}\left(1 - \frac{\sin^2\epsilon_\theta}{2}\right)\boldsymbol{G} - \frac{\mu_\oplus(1+\epsilon_r)}{R^3}\boldsymbol{P} - \left(\frac{\epsilon_r}{\tau_{m1}^2} + \frac{\dot{\epsilon}_r}{\tau_{m2}}\right)\boldsymbol{I} - \frac{\dot{\theta}_c}{\tau_{m3}}\boldsymbol{G}\right)\vec{u}_r, \tag{55}$$

$$\ddot{\theta}_t = -\frac{\dot{\epsilon}_a}{\tau_t}\frac{1 - \frac{3}{4}\sin^2\epsilon_\theta}{(1+\epsilon_r)^6}, \tag{56}$$

$$\ddot{\theta}_c = -\frac{1}{\tau_c}\frac{\dot{\epsilon}_a}{(1+\epsilon_r)^6} + \frac{\epsilon_\theta}{\tau_{m4}^2} + \frac{\dot{\epsilon}_\theta}{\tau_{m5}}, \tag{57}$$

where the matrix $\boldsymbol{P}$ and the matrix $\boldsymbol{G}$ are equal to,

$$\boldsymbol{P} = \begin{bmatrix} 1 - 3\cos^2\theta_R & -3\cos\theta_R\sin\theta_R \\ -3\cos\theta_R\sin\theta_R & 1 - 3\sin^2\theta_R \end{bmatrix}, \quad \boldsymbol{G} = \begin{bmatrix} 0 & -1 \\ 1 & 0 \end{bmatrix}, \tag{58}$$

and the characteristic times τ_r, τ_c, τ_t given by Equations (80, 83, 78) depend on the physical properties of the chaser and the target.

In order to analyze the stability of the system, a hypothetical stable asymptotic state is assumed with $\epsilon_r \to 0$, $\epsilon_\theta \to 0$, $\epsilon_a \to 0$ and $\dot{\theta}_c \to 0$. The variable ϵ_a will tend to zero when the de-tumbling process is close to its end.

Equations (55, 56, 57) depend on the control variables and they are linearized as follows. First of all, combining Equations (56) and (57) and neglecting infinitesimals of second order, the linearized equation in ϵ_a is obtained,

$$\ddot{\epsilon}_a = \ddot{\theta}_t - \ddot{\theta}_c = (\frac{1}{\tau_c} - \frac{1}{\tau_t})\dot{\epsilon}_a - \frac{\epsilon_\theta}{\tau_{m4}^2} - \frac{\dot{\epsilon}_\theta}{\tau_{m5}}. \tag{59}$$

Secondly, in order to find the differential equation for ϵ_r and ϵ_θ, the following relationship is used,

$$\frac{\vec{r}}{d} = \boldsymbol{R_c}\vec{\epsilon} + \begin{bmatrix} \cos\theta_c \\ \sin\theta_c \end{bmatrix}, \tag{60}$$

where the variables ϵ_r and ϵ_θ have been grouped in a single vector $\epsilon = \begin{bmatrix} \epsilon_r \\ \epsilon_\theta \end{bmatrix}$ and where $\boldsymbol{R_c}$ is equal to

$$\boldsymbol{R_c} = \begin{bmatrix} \cos\theta_c & -\sin\theta_c \\ \sin\theta_c & \cos\theta_c \end{bmatrix}.$$

Taking second derivatives with respect to time of both sides of Equation (60) results in

$$\frac{\ddot{\vec{r}}}{d} = \boldsymbol{R_c}\ddot{\vec{\epsilon}} + 2\dot{\theta}_c\boldsymbol{R'_c}\dot{\epsilon} + (\ddot{\theta}_c\boldsymbol{R'_c} - \dot{\theta}_c^2\boldsymbol{R_c})\vec{\epsilon} - \begin{bmatrix} \ddot{\theta}_c\sin\theta_c + \dot{\theta}_c^2\cos\theta_c \\ -\ddot{\theta}_c\cos\theta_c + \dot{\theta}_c^2\sin\theta_c \end{bmatrix}, \tag{61}$$

where the following time derivatives of $\boldsymbol{R_c}$ have been used,

$$\dot{\boldsymbol{R}}_c = \dot{\theta}_c\boldsymbol{R'_c} = \dot{\theta}_c\begin{bmatrix} -\sin\theta_c & -\cos\theta_c \\ \cos\theta_c & -\sin\theta_c \end{bmatrix}, \quad \ddot{\boldsymbol{R}}_c = \ddot{\theta}_c\boldsymbol{R'_c} + \dot{\theta}_c^2\boldsymbol{R''_c} = \ddot{\theta}_c\boldsymbol{R'_c} - \dot{\theta}_c^2\boldsymbol{R_c}. \tag{62}$$

Neglecting infinitesimals of second order, Equation (61) is equal to,

$$\frac{\ddot{\vec{r}}}{d} = \boldsymbol{R_c}\ddot{\vec{\epsilon}} + \ddot{\theta}_c \begin{bmatrix} -\sin\theta_c \\ \cos\theta_c \end{bmatrix} \rightarrow \ddot{\vec{\epsilon}} - \boldsymbol{R_c}^{-1}\frac{\ddot{\vec{r}}}{d} + \ddot{\theta}_c \boldsymbol{R_c}^{-1} \begin{bmatrix} -\sin\theta_c \\ \cos\theta_c \end{bmatrix} = \vec{0}, \tag{63}$$

where the following relationships have been used,

$$\boldsymbol{R_c}^{-1}\vec{u}_r = \begin{bmatrix} 1 \\ 0 \end{bmatrix}, \quad \boldsymbol{R_c}^{-1}\boldsymbol{G}\vec{u}_r = \begin{bmatrix} 0 \\ 1 \end{bmatrix}. \tag{64}$$

Now combining Equations (55) and (63), the following differential equation in $\vec{\epsilon}$ is derived,

$$\ddot{\vec{\epsilon}} + \begin{bmatrix} \frac{\epsilon_r}{\tau_{m1}^2} + \frac{\dot{\epsilon}_r}{\tau_{m2}} + P_1\epsilon_r + P_2\epsilon_\theta \\ -\dot{\epsilon}_a(\frac{1}{\tau_r} + \frac{1}{\tau_c}) + \frac{\epsilon_\theta}{\tau_{m4}^2} + \frac{\dot{\epsilon}_\theta}{\tau_{m5}} + \frac{\dot{\theta}_c}{\tau_{m3}} + P_2\epsilon_r + P_3\epsilon_\theta \end{bmatrix} = -\frac{\mu_\oplus}{R^3} \begin{bmatrix} P_1 \\ P_2 \end{bmatrix}, \tag{65}$$

where,

$$P_1 = \frac{\mu_\oplus}{R^3}(1 - 3\cos^2(\theta_c - \theta_R)), \quad P_2 = \frac{3}{2}\frac{\mu_\oplus}{R^3}\sin 2(\theta_c - \theta_R), \quad P_3 = \frac{\mu_\oplus}{R^3}(1 - 3\sin^2(\theta_c - \theta_R)). \tag{66}$$

Finally, the linearized differential equations for the control variables can be expressed in the matrix form $\boldsymbol{A}\ddot{\vec{Z}} + \boldsymbol{B}\dot{\vec{Z}} + \boldsymbol{C}\vec{Z} = \boldsymbol{D}$,

$$\begin{bmatrix} 1 & 0 & 0 & 0 \\ 0 & 1 & 0 & 0 \\ 0 & 0 & 1 & 0 \\ 0 & 0 & 0 & 0 \end{bmatrix}\ddot{\vec{Z}} + \begin{bmatrix} \frac{1}{\tau_{m2}} & 0 & 0 & 0 \\ 0 & \frac{1}{\tau_{m5}} & -(\frac{1}{\tau_r} + \frac{1}{\tau_c}) & 0 \\ 0 & \frac{1}{\tau_{m5}} & \frac{1}{\tau_t} - \frac{1}{\tau_c} & 0 \\ 0 & -\frac{1}{\tau_{m3}} & \frac{1}{\tau_c} & 1 \end{bmatrix}\dot{\vec{Z}} + \begin{bmatrix} \frac{1}{\tau_{m1}^2} + P_1 & P_2 & 0 & 0 \\ P_2 & \frac{1}{\tau_{m4}^2} + P_3 & 0 & \frac{1}{\tau_{m3}} \\ 0 & \frac{1}{\tau_{m4}^2} & 0 & 0 \\ 0 & -\frac{1}{\tau_{m4}^2} & 0 & 0 \end{bmatrix}\vec{Z} = -\frac{\mu_\oplus}{R^3}\begin{bmatrix} P_1 \\ P_2 \\ 0 \\ 0 \end{bmatrix}. \tag{67}$$

In order to apply the Laplace transformation, the four matrices should be constant; however the parameters $R(t)$ and $P_i(\theta_R, \theta_c)$ vary with time. As a first approximation, this time variation can be neglected. The orbital period $\tau_\oplus = \frac{2\pi R^3}{\mu_\oplus}$ is of the order of one hour in LEO and 1 day in GEO, while the period of the angular rotation of the target object is of the order of seconds. Therefore, the evolution of the COG of the system, given by $R(t), \theta_R(t)$, is slow compared to the angular velocity of the target object. In addition, the control will guarantee that $\dot{\theta}_c \rightarrow 0$ and therefore, $\theta_c \approx constant$ in the vicinity of the equilibrium state.

Assuming null initial conditions, the Laplace transformation is now used to derive the characteristic equation $|\boldsymbol{\Delta}(s)| = 0$ as the condition for existence of solutions $\delta\vec{Z} \neq \vec{0}$ around a hypothetical equilibrium state $\vec{Z}$ that

verifies Equation (67) with $\boldsymbol{A}, \boldsymbol{B}, \boldsymbol{C}, \boldsymbol{D} \approx constants$ [45],

$$\boldsymbol{\Delta}(s) = s^2 \boldsymbol{A} + s\boldsymbol{B} + \boldsymbol{C}. \tag{68}$$

The roots of the determinant $|\boldsymbol{\Delta}(s)|$ will indicate the stability of the system in the vicinity of the equilibrium position defined. If the roots have any real positive parts, this may lead to an instability in the control process [46]. In general, the inverses of the characteristic times for the maneuvers will dominate over the rest of the characteristic times that appear in the problem $\tau_{mi} << \tau_r, \tau_c, \tau_t, \tau_\oplus$. One conclusion derived from this analysis is that the selection of the τ_{mi} is of paramount importance in order to guarantee, at least, local stability. In order to test the validity of this control strategy for the full 3D dynamical problem, several case studies are presented in Section V.

Here, an example is presented which shows that the results derived from the linear stability analysis may not be conclusive. The target analyzed is a metallic spherical shell, made of aluminum, which has a radius of 1 meter and a thickness of 3 millimeters. Its magnetic tensor, assuming an efficiency loss of a 5%, is equal to [22],

$$\boldsymbol{M}_{Sphere} = \begin{bmatrix} 3.343 & 0 & 0 \\ 0 & 3.343 & 0 \\ 0 & 0 & 3.343 \end{bmatrix} \cdot 10^6 \text{ S} \cdot \text{m}^4. \tag{69}$$

The chaser that carries the de-tumbling subsystem is the spacecraft designed for the Agora mission [19]. This spacecraft has a dry mass equal to $m_c = 1402$ kg and its principal moments of inertia are $I_{cx} = 2128$ kg·m^2, $I_{cy} = 2128$ kg·m^2, $I_{cz} = 1631$ kg·m^2 [19].

Both objects are located at a circular orbit of 800 km of altitude and 0 degrees of inclination and the relative distance between the coil and the COG of the target object is 10 meters (see Figure 5). Moreover, the chaser points the magnetic moment of the coil towards the target object to maximize the magnetic field ($\epsilon_\theta = 0$). In addition, the initial angular velocity of the target with respect to the ECI frame is equal to $\vec{\omega} = [0, 0, 10]$ deg/s.
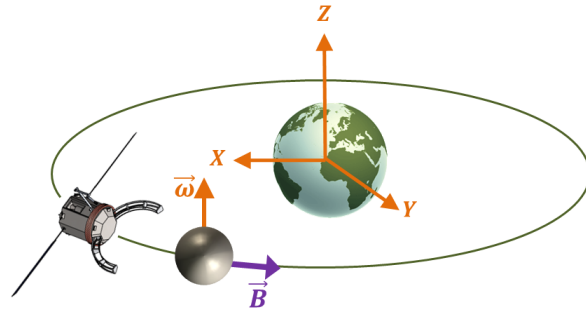
Figure 5: Initial configuration for de-tumbling process of a spherical shell.

Using the following characteristic times $\tau_{m1} = 5\text{s}$, $\tau_{m2} = 1000\text{s}$, $\tau_{m3} = 500\text{s}$, $\tau_{m4} = 0.1\text{s}$, $\tau_{m5} = 0.1\text{s}$, the roots of the determinant $|\mathbf{\Delta}(s)|$ are equal to,

- $s_1 = 0$, $s_{2,3} = -4.9 \pm 8.7i$, $s_{4,5} = -0.0005 \pm 0.2i$, $s_6 = -0.002$, $s_7 = -0.00002$.

In this particular case, the stability analysis indicates that the system is locally marginally stable as there is one pole with a zero real part which is a simple root and the rest of the poles have a negative real part. Here, it is impossible to know by inspection whether the full dynamical process will become unstable or not.

Now the dynamical Equations (47) are numerically integrated in order to assess the global stability of the system. The numerical simulation includes the Earth modeled as a point mass, the magnetic interactions between the two objects and the control maneuvers. In addition, it is assumed that there are neither delays nor inaccuracies in the control process.

The evolution of the control parameters; angular velocity of the target and the chaser, the relative distance between the two objects and the relative pointing of the coil, are depicted in Figure 6. The results show that the selected τ_{mi} lead to a stable control throughout the whole de-tumbling process.
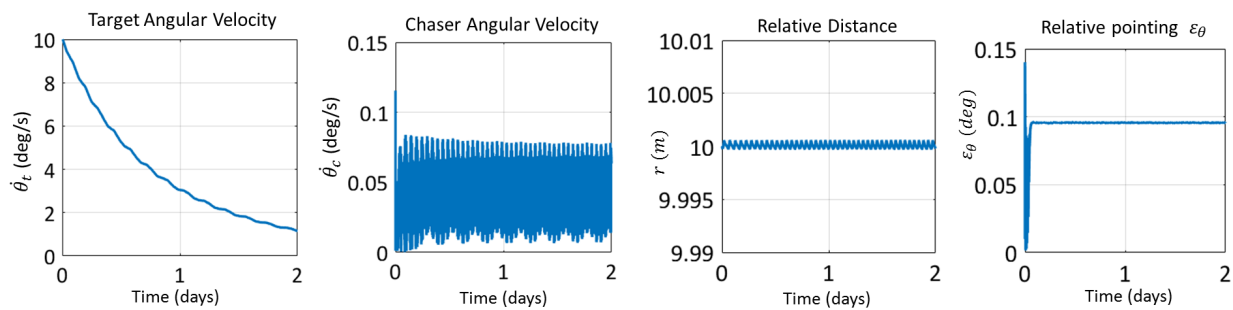
Figure 6: Kinematics of the chaser-target system.

American Institute of Aeronautics and Astronautics

All in all, the linear stability analysis sheds some light over the local behavior of the system but it does not ensure that the conclusions derived are valid for the whole dynamical process and the linear analysis must always be complemented by numerical simulations. Therefore, the presented linear analysis is a heuristic tool but it is not conclusive for practical purposes.

Moreover, an optimization criteria based on the minimization of the total ΔV is identified as an efficient way to find adequate values of the τ_{mi}. However, the large amount of possible combinations between the 5 variables τ_{mi} leads to a complicated optimization process. In this case, the stability analysis can be a useful tool in order to make an educated initial guess of the variables τ_{mi}.

V. Case studies

The following case studies consider an Ariane-4 H10 and an Ariane-5 EPS upper stages as target objects (see Figure 7). Currently, there are more than 120 Ariane rocket bodies in orbit, primarily in Geostationary Transfer Orbit (GTO) and LEO, which pose a sizable risk to other objects in space [19]. The large fraction of conductive materials within an Ariane-4 rocket body makes it suitable for the application of the Eddy Brake method.

In this section the 3D dynamical Equations (47) are numerically integrated including the effect of the Earth's gravity modeled as a point mass, the magnetic interactions between the two objects and the control maneuvers. The integration method employed is a Runge-Kutta of fourth order with a constant time step of 1 second [47] and the integration process is further explain in the Annex VI. A delay of $\tau = 2$ seconds and an inaccuracy 1% have been taken into account, based on average values of possible inaccuracies and delays introduced by sensors and actuators (see Subsection C of Section III).

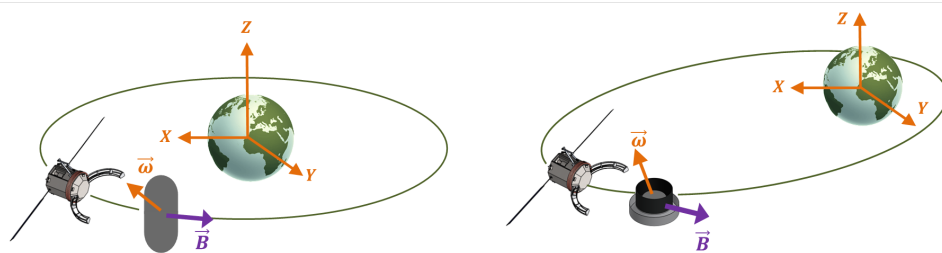The chaser employed for these case studies is the spacecraft designed for the Agora mission [19].

Figure 7: Initial configuration for Ariane-4 (left image) and the Ariane-5 (right image).

In both case studies, an optimization process of the total ΔV has been carried out given by the objective

American Institute of Aeronautics and Astronautics

function (42) in which the search space of the characteristic times has been restricted to $\tau_{mi} = [0.0001, 5000]$ s. For the ΔV computation, it has been considered that the torque is generated by two thrusters separated by a distance of $d_{th} = 1.65$ meters.

Furthermore, the efficiency factor μ_{eff} needs to be selected in the model for the losses derived from the non-uniformity of the field. This parameter depends on the size of the target, the size of the coil and the relative distance and an efficiency factor of 95% has been considered as an adequate value for these case studies [22].

A.   1st case study: Ariane-4 upper stage

This case study analyzes a generic 3D dynamical problem for an Ariane-4 rocket body. The mass of the Ariane-4 upper stage, considered is 2154 kg and the principal moments of inertia of the target are $I_{tx} = 28000$ kg·m², $I_{ty} = 28000$ kg·m², $I_{tz} = 3000$ kg·m² [22, 48]. Ariane-4 rocket bodies have two concentric aluminum tanks, which have a cylindrical central part and two hemispherical bulkheads and these have been used to model the Magnetic Tensor. The total conductive material computed is approximately 32% of the overall mass [48]. The magnetic tensor, expressed in its body reference frame, employed for this object is equal to [22],

$$\boldsymbol{M}_{Ariane4} = \begin{bmatrix} 5.908 & 0 & 0 \\ 0 & 5.908 & 0 \\ 0 & 0 & 1.951 \end{bmatrix} \cdot 10^6 \text{ S} \cdot \text{m}^4. \tag{70}$$

The initial angular velocity of its body frame with respect to the ECI frame is equal to $\vec{\omega} = [5.8, 5.8, 5.8]$ deg/s ($|\vec{\omega}| = 10$ deg/s). The initial orbit is a circular orbit at 700 km of altitude and 0 degrees of inclination and the relative distance between the coil and the COG of the target object is 10 meters (see Figure 7). Moreover, the chaser points the magnetic moment of the coil towards the target object to maximize the magnetic field ($\epsilon_\theta = 0$).

The characteristic times of the control maneuvers derived from the optimization process are $\tau_{m1} = 20$s, $\tau_{m2} = 2000$s, $\tau_{m3} = 700$s, $\tau_{m4} = 2$s, $\tau_{m5} = 0.0001$s and the total ΔV needed to decrease the angular velocity from $\omega_0 = 10$ deg/s to $\omega_f = 3$ deg/s is $\Delta V = 20.24$ m/s.

Figure 8 shows the evolution of the kinematic variables involved in the control. First of all, the evolution of the angular velocity of the target is depicted. It can be observed that the component ω_z, perpendicular to the orbital plane of the target, decreases much faster than the two other components. This is due to the fact that this component is always perpendicular to the magnetic field generated by the target while the other two components continuously vary their relative configuration with respect to the magnetic field throughout

American Institute of Aeronautics and Astronautics

each orbital period. In addition, the inertial angular velocity of the chaser, the relative distance and the relative pointing of the coil are successfully controlled during the de-tumbling process as shown in Figure 8.
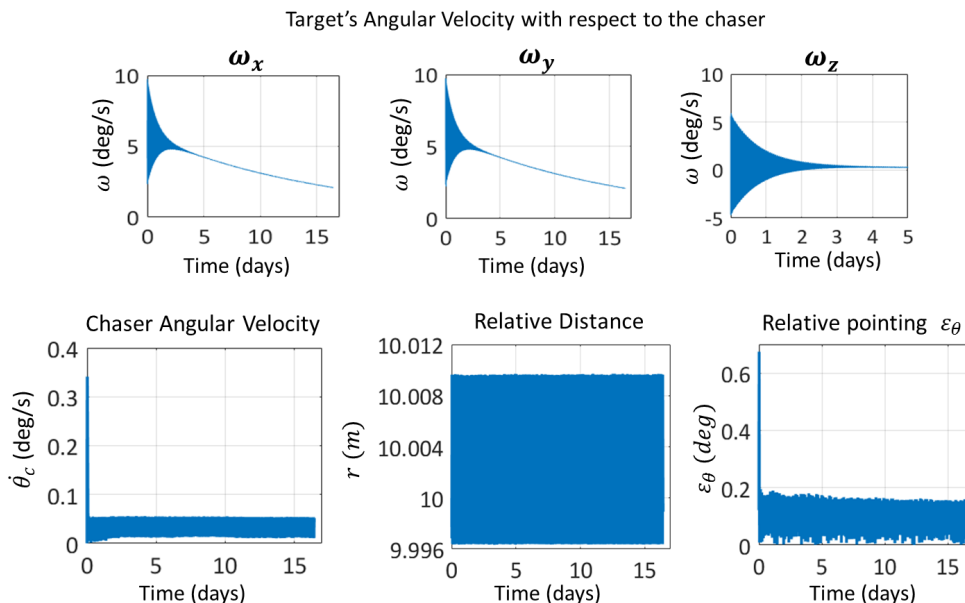

Figure 8: Kinematics of the chaser-target system.

Furthermore, Figure 9 depicts the evolution of the maneuvers executed by the chaser. It can be observed that there is a transient stage at the beginning of the process, where peak values of the forces and torques are reached. This transient state appears due to the fact that the initialization of the magnetic field follows a step function. However, only the asymptotic behavior is relevant for the stability analysis. After this stage, the necessary forces and torques throughout the de-tumbling process stay in the range of tens of milliNewtons and tens of milliNewtons per meter respectively. The most fuel consuming maneuvers are the forces needed to keep a constant relative distance.
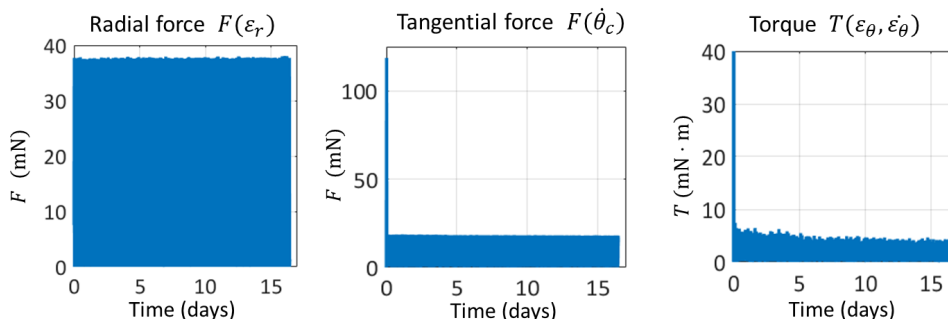
Figure 9: Maneuvers exerted by the chaser.

American Institute of Aeronautics and Astronautics

Finally, Figures 10 and 11 depict the evolution of the semimajor axis, eccentricity and inclination of the target and the chaser. It is observed that the magnetic interactions primarily change the semimajor axis of the orbits and therefore, the relative motion control is largely restricted to planar relative positioning.
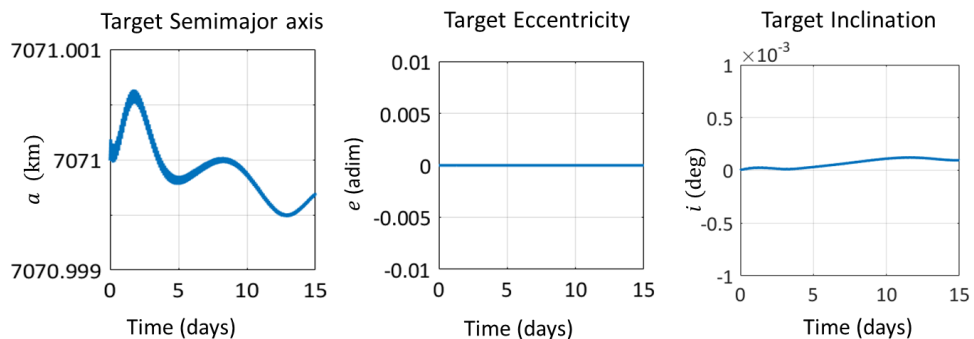

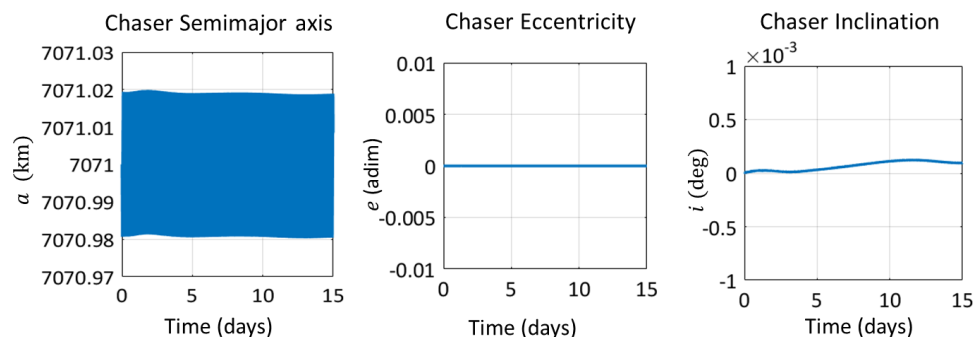Figure 10: Semimajor axis, eccentricity and inclination of the target.

Figure 11: Semimajor axis, eccentricity and inclination of the chaser.

B. 2nd case study: Ariane-5 EPS

This case study analyzes a generic 3D dynamical problem for an Ariane-5 EPS upper stage (EPS: Etage Propergols Stockables). The mass of the rocket body considered is 3055.3 kg and the principal moments of inertia of the target are $I_{tx} = 11148$ kg·m^2, $I_{ty} = 8058$ kg·m^2, $I_{tz} = 6479$ kg·m^2 [49]. The conductive components taken into account for the generation of the eddy currents are the four aluminum propellant tanks of the EPS. The total percentage of conductive mass versus the total mass of the target is 8.8%. The magnetic tensor, expressed in its body reference frame, employed for this object is equal to [19],

$$
\boldsymbol{M}_{Ariane5} = \begin{bmatrix} 1.73 & 0 & 0 \\ 0 & 1.73 & 0 \\ 0 & 0 & 1.73 \end{bmatrix} \cdot 10^5 \text{ S} \cdot \text{m}^4.
\tag{71}
$$

American Institute of Aeronautics and Astronautics

The initial angular velocity of its body frame with respect to the ECI frame is equal to $\vec{\omega} = [6, 4, 7]$ deg/s. The initial orbit is GTO, with an apogee altitude of 35786 km and a perigee of 250 km and the relative distance between the coil and the COG of the target object is 10 meters (see Figure 7). In addition, the chaser points the magnetic moment of the coil towards the target object to maximize the magnetic field ($\epsilon_\theta = 0$).

In this case, the following characteristic times of the control maneuvers are obtained, $\tau_{m1} = 50$s, $\tau_{m2} = 3000$s, $\tau_{m3} = 3000$s, $\tau_{m4} = 5$s, $\tau_{m5} = 0.0001$s. The total ΔV needed to decrease the angular velocity from $\omega_0 = 10$ deg/s to $\omega_f = 6$ deg/s is $\Delta V = 17.6$ m/s. In this specific case, it would take approximately four months to decrease the angular velocity to between 4 deg/s which is an acceptable threshold for some robotic manipulators to grab big derelicts [7, 8, 9]. Figure 12 depicts the evolution of the norm of the angular velocity of the target and the chaser, the relative distance between the two objects and the relative pointing of the coil which are successfully controlled. In this case study, the time needed for the de-tumbling process is longer than the previous case due to the fact that the target has less amount of conductive material. In addition, Figure 13 shows the maneuvers executed by the chaser which are in the order of tens of milliNewtons and milliNewtons per meter. Peak values are reached in the vicinity of the perigee of each orbit due to the fact that the two objects move at a faster pace than at the apogee.
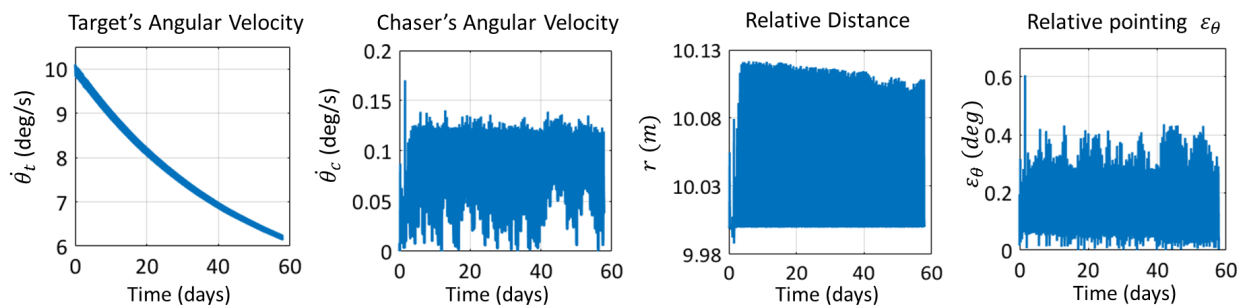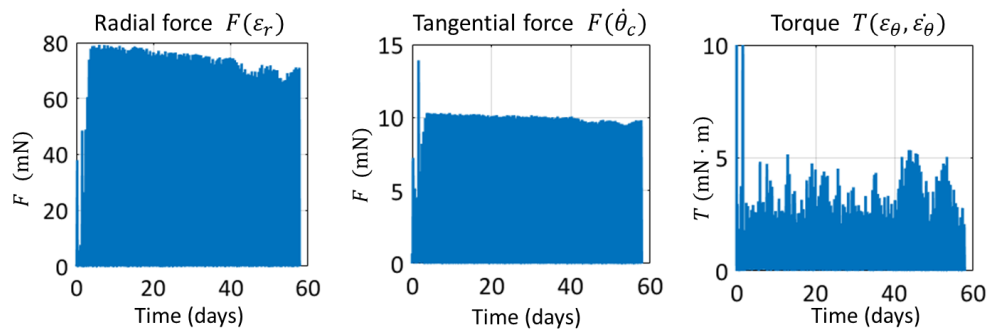

Figure 12: Kinematics of the chaser-target system.

Figure 13: Maneuvers exerted by the chaser.

American Institute of Aeronautics and Astronautics

Finally, Figures 14 and 15 depict the evolution of the semimajor axis, eccentricity and inclination of the target and the chaser. Analogously to the previous case study, the magnetic interactions primarily change the semimajor axis of the orbits while the eccentricity and the inclination hardly change. Therefore, the relative motion control is largely restricted to planar relative positioning.
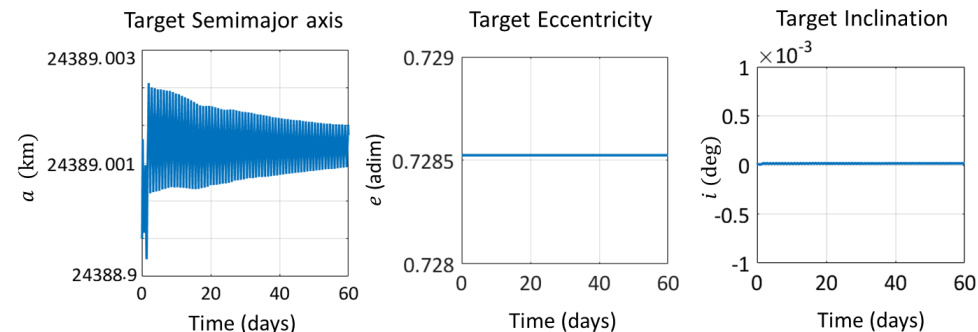

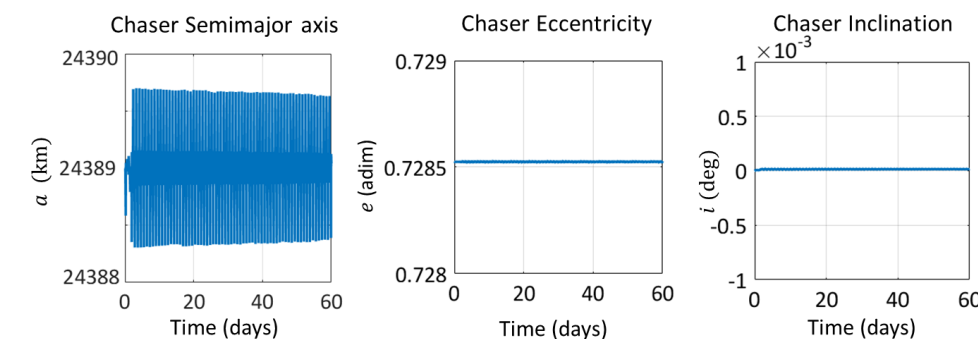Figure 14: Semimajor axis, eccentricity and inclination of the target.

Figure 15: Semimajor axis, eccentricity and inclination of the chaser.

VI.   Conclusions

The present article focuses on the guidance, navigation and control subsystem for a contactless de-tumbling method for space debris objects ('Eddy Brake').

First of all, among the two relevant pointing configurations identified, it has been concluded that configuration ($\perp$) is less attractive than configuration ($\parallel$). This is due to the fact that this configuration is dependent on the angular velocity and the magnetic tensor of the target which would lead to very complex operations for longer periods of time than configuration ($\parallel$).

Secondly, based on the main requirements for the pose estimation sensors needed for the 'Eddy Brake', the flash lidar has been identified as the most adequate sensor. This is due to the procured sensor range and

American Institute of Aeronautics and Astronautics

field of view, its range and attitude accuracies, its robustness with respect to the illumination conditions, its capacity to capture rapid changing scenes and its reliability.

Furthermore, the 3D numerical integration process of the chaser-target system is a complex problem as it includes a set of non-linear differential equations where the linear and rotational dynamics of the two objects are coupled. The complexity of the problem increases when adding inaccuracies and delays in the control derived from the sensors and actuators which can easily lead to instabilities unless proper control maneuvers are included.

Moreover, it has been verified that the design of the control maneuvers based on a first analysis of a simplified 2D problem has been an appropriate strategy. Within this analysis, four variables were identified as the minimum number of control variables necessary to meet the aforementioned requirements; the relative distance, the error in the relative pointing, the relative angular velocity of the target and the inertial angular velocity of the chaser.

In addition, the generalized 3D control strategy based on a proportional-derivative control has been tested and validated for two different case studies; the de-tumbling of an the Ariane-4 and an Ariane-5 upper stages. These results show a successful control of the chaser-target system throughout the full dynamical process.

Finally, it has been identified that the stability of the control throughout the de-tumbling process depends primarily on the adequate selection of the characteristic times of the maneuvers τ_{mi}. A criterion to select these parameters, based on the minimization of the total ΔV of the de-tumbling process, has proven to be very effective for the case studies presented. However, the large amount of possible combinations between the variables τ_{mi} leads to a complicated optimization process. A simplified 2D analytical study in the vicinity of the final equilibrium state has also been included and it sheds some light over the effect of the characteristic times of the control maneuvers in the stability of the system. Although the conclusions of the linear analysis can not be exported to the full dynamical problem, it has been shown that it can be a useful tool to make an educated initial guess of the variables τ_{mi} in the optimization process.

Appendix

Magnetic dipole formulation and comparison with MTT

In this section the formula of the force based on the Magnetic Tensor Theory (Eq. 7) is compared with the magnetic dipole approximation (Eq. 10). The magnetic field produced by a magnetic dipole which has a

magnetic moment equal to $\vec{m}$ is [42],

$$\vec{B} = \frac{\mu_0}{4\pi}\left[\frac{3(\vec{m}\cdot\vec{r})\cdot\vec{r}}{r^5} - \frac{\vec{m}}{r^3}\right]. \tag{72}$$

where $\mu_0 = 4\pi \cdot 10^{-7}$ NA^{-2} is the vacuum permeability and $\vec{r}$ the position vector and the force between two magnetic dipoles is [42],

$$\vec{F} = \frac{3\mu_0}{4\pi r^5}\left((\vec{m}_t\cdot\vec{r})\vec{m}_c + (\vec{m}_c\cdot\vec{r})\vec{m}_t + (\vec{m}_c\cdot\vec{m}_t)\vec{r} - \frac{5(\vec{m}_t\cdot\vec{r})(\vec{m}_c\cdot\vec{r})}{r^2}\vec{r}\right), \tag{73}$$

where $\vec{m}_t$ and $\vec{m}_c$ are the magnetic dipoles of the target and the chaser and $\vec{r}$ is the relative state vector between the two objects.

The force will be evaluated for a coil that is pointing towards the COG of the target object (configuration ($\parallel$)). In addition, the target object is considered to be an aluminum spherical shell of the following characteristics; the radius of the target is equal to $R_t = 2$ m, the thickness is equal to $e_t = 1$ mm, the electrical conductivity considered is $\sigma_t = 3.5e7$ S/m and the angular velocity is $\dot{\epsilon}_a = 50$ deg/s. The coil on-board the chaser spacecraft has the properties defined in Section II.

Figure 16 shows the force computed using both models. The magnetic dipole force better approximates the force given by the Equation (7) when the distance between the two objects increases. In addition, the force given by the magnetic dipole approximation overvalues the generated force. Furthermore, the magnetic
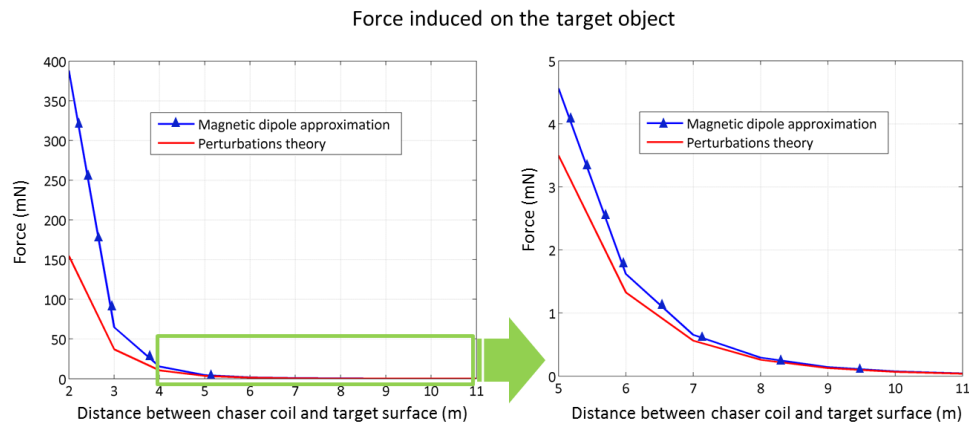

Figure 16: Force model comparison between perturbations theory and the magnetic dipole model for different relative distances.

dipole approximation does not take into account variations in the non-uniformity of the magnetic field. When the radius of the coil increases, the magnetic field becomes more uniform inside the target object and therefore, the force must decrease. This phenomenon is not well characterized by the magnetic dipole

approximation as the force increases when it should decrease. In order to visualize the difference between the two models, the following properties have been considered, a magnetic field at the COG of the target equal to $B_{Gt} = 150 \ \mu$T and a relative distance between the coil and the COG of the target of 10 meters.

Figure 17 shows the magnetic field foreseen by both models when the radius of the coil varies. The magnetic field at the COG of the target is assumed to be constant and the intensity of the coil is adjusted accordingly to have the same field in all the cases.
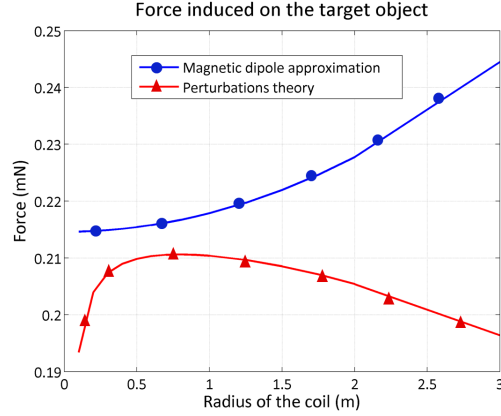

Figure 17: Force model comparison between perturbations theory and the magnetic dipole model for different radii of the coil.

Magnetic interactions between a chaser and a metallic spherical shell in the 2D dynamical problem

In the 2D configuration, the chaser and the spherical target are assumed to move in coplanar orbits and be able to rotate about an axis perpendicular to the orbit. The following reference frame is used here, the origin of the frame is located at the COG of the chaser, the X axis goes along the $\vec{u}_r$ direction, the Z axis is parallel to the angular momentum of the orbital plane and the Y axis goes along the direction $\vec{u}_{r\perp} = \vec{k} \times \vec{u}_r = \boldsymbol{G}\vec{u}_r$.

In this configuration, the magnetic moment vector of the coil $\vec{m}_c$ on-board the chaser is,

$$\vec{m}_c = |\vec{m}_c| \left(\cos(\epsilon_\theta)\vec{u}_r + \sin(\epsilon_\theta)\boldsymbol{G}\vec{u}_r\right). \tag{74}$$

Introducing Equation (74) in (72), the magnetic field generated by the coil is,

$$\vec{B} = \frac{\mu_0 |\vec{m}_c|}{4\pi r^3} \left(2\cos(\epsilon_\theta)\vec{u}_r - \sin(\epsilon_\theta)\boldsymbol{G}\vec{u}_r\right). \tag{75}$$

Furthermore, the magnetic moment of a rotating metallic spherical shell subject to an external magnetic

American Institute of Aeronautics and Astronautics

field is [22],

$$\vec{m}_t = \boldsymbol{M}_{\text{eff}}(\dot{\epsilon}_a \vec{k} \times \vec{B}_{Gt}) = \frac{2\pi}{3} \mu_{\text{eff}} \sigma_t R_t^4 e_t (\dot{\epsilon}_a \vec{k} \times \vec{B}_{Gt}), \tag{76}$$

where μ_{eff} is an efficiency factor included due to the fact that the field inside the target is non-uniform, σ_t is the conductivity of the spherical shell, R_t and e_t are the radius and thickness of the target, $\dot{\epsilon}_a \vec{k}$ is the relative angular velocity of the target with respect to the chaser and $\vec{B}_{Gt}$ is the magnetic field at the COG of the target object.

Introducing Equation (74) in (6), the following formula for the eddy current torque is obtained,

$$\vec{T}_{ct} = -\frac{I_{tz}}{\tau_t} \dot{\epsilon}_a \frac{1 - \frac{3}{4} \sin^2 \epsilon_\theta}{(1 + \epsilon_r)^6} \vec{k}, \tag{77}$$

where I_{tz} is the principal inertia of the target along the Z axis (which is equal for all axis in a spherical shell) and the characteristic time τ_t is equal to,

$$\tau_t = \frac{6 d^6 \pi I_{tz}}{\mu_0^2 \mu_{\text{eff}} \sigma_t R_t^4 e_t |\vec{m}_c|^2}. \tag{78}$$

Moreover, introducing Equations (74, 75, 76) in Equation (73), the force that appears at the COG of the target object is evaluated,

$$\vec{F}_{ct} = \frac{m_{red} d}{\tau_r} \dot{\epsilon}_a \frac{(1 - \frac{\sin^2 \epsilon_\theta}{2})}{(1 + \epsilon_r)^7} \boldsymbol{G} \vec{u}_r, \tag{79}$$

where the characteristic time of the force τ_r is equal to,

$$\tau_r = m_{red} \frac{4\pi d^8}{\mu_0^2 \mu_{\text{eff}} \sigma_t R_t^4 e_t |\vec{m}_c|^2}. \tag{80}$$

The reactions on the chaser are given by Equations (8, 9) and for this specific problem, they acquire the form,

$$\vec{F}_{tc} = -\frac{m_{red} d}{\tau_r} \dot{\epsilon}_a (1 - \frac{\sin^2 \epsilon_\theta}{2}) \boldsymbol{G} \vec{u}_r, \tag{81}$$

$$\vec{T}_{tc} = -\frac{I_{cz}}{\tau_c} \frac{\dot{\epsilon}_a}{(1 + \epsilon_r)^6} \vec{k}, \tag{82}$$

where the characteristic time of the magnetic torque on the chaser τ_c is equal to,

$$\tau_c = \frac{12\pi d^6 I_{cz}}{\mu_0^2 \mu_{\text{eff}} \sigma_t R_t^4 e_t |\vec{m}_c|^2}. \tag{83}$$

American Institute of Aeronautics and Astronautics

Integration of the 3D dynamical equations

The general dynamical equations of the de-tumbling process include 24 non-linear first order differential equations (12 equations for the chaser and 12 equations for the target). In this section, the general differential equations to describe the translational and rotational motion of a rigid body are described as well as their integration process. The subindex in indicates that the variable is expressed in an inertial reference frame and subindex b denotes that the variable is expressed in the body reference frame. The state vector that represents the translational and rotational kinematics of a rigid body have been represented by the vector $\vec{y}$,

$$\vec{y} = \begin{bmatrix} \vec{r}_{in} \\ \vec{v}_{in} \\ \vec{\alpha}_{in} \\ \vec{\omega}_b \end{bmatrix}. \tag{84}$$

Vectors $\vec{r}_{in}$ and $\vec{v}_{in}$ are the inertial position and velocity of the object and they describe the translational kinematics of the object. Moreover, vector $\vec{\omega}_b$ is the rotational velocity vector of the body frame with respect to the inertial reference frame expressed in the body frame and the components of vector $\vec{\alpha}_{in} = \alpha \vec{h}$ are the Euler parameters used to describe the attitude of the object. If a rigid body is rotating with an angular velocity $\vec{\omega}_b$, this rotation can always be represented by a rotation angle α around a certain axis $\vec{h}$. These four variables $(\alpha, \vec{h})$ are called Euler parameters [44].

The translational dynamical equations are governed by Newton's second law. In addition, the rotational dynamics are determined using Euler's equations and the differential equation for $\vec{\alpha}_{in}$ is given by Equation (85) [44],

$$\dot{\vec{\alpha}}_{in} = \vec{\omega}_{in} + \frac{\alpha}{2}(\vec{\omega}_{in} \times \vec{h}_{in} + \frac{\alpha^2}{12}(\vec{h}_{in} \times (\vec{h}_{in} \times \vec{\omega}_{in})) + o(\alpha^3) = f(\alpha, \vec{h}_{in}, \vec{\omega}_{in}). \tag{85}$$

Hence, the system of non-linear differential equations that needs to be solved for each body is equal to,

$$\dot{\vec{y}} = F(t, \vec{y}(t)) \rightarrow \begin{bmatrix} \dot{\vec{r}}_{in} \\ \dot{\vec{v}}_{in} \\ \dot{\vec{\alpha}}_{in} \\ \dot{\vec{\omega}}_b \end{bmatrix} = \begin{bmatrix} \vec{v}_{in} \\ \sum \vec{F}_{ext} \\ f(\alpha, \vec{h}_{in}, \vec{\omega}_{in}) \\ \mathbf{I}^{-1}(\sum \vec{T}_{ext} - (\vec{\omega}_b \times \mathbf{I}\vec{\omega}_b)) \end{bmatrix}, \tag{86}$$

where $\sum \vec{F}_{ext}$ and $\sum \vec{T}_{ext}$ are the sum of all the external forces and torques acting upon the object, including the environmental perturbations and the maneuvers for the control.

American Institute of Aeronautics and Astronautics

Furthermore, in each time step of the integration process $\Delta t = t - t_0$, the rotation matrix between the body frame and the inertial reference frame, $R(t)$, is computed as the composition of two rotation matrices; the rotation matrix $R(t_0)$ between the beginning of the simulation $t = 0$ and the initial time in the propagation step t_0 and the rotation matrix $A(\alpha_{in}(t))$ which gives the rotation during that timestep $t' \in [t_0, t]$ [44],

$$R(t) = A(\alpha_{in}(t)) \cdot R(t_0), \tag{87}$$

where the matrix $A(\alpha_{in}(t))$ has the form [44],

$$A = \begin{bmatrix} (1 - \cos(\alpha_{in}))h_x^2 + \cos(\alpha_{in}) & (1 - \cos(\alpha_{in}))h_x h_y - h_z \sin(\alpha_{in}) & (1 - \cos(\alpha_{in}))h_x h_z + h_y \sin(\alpha_{in}) \\ (1 - \cos(\alpha_{in}))h_x h_y + h_z \sin(\alpha_{in}) & (1 - \cos(\alpha_{in}))h_y^2 + \cos(\alpha_{in}) & (1 - \cos(\alpha_{in}))h_y h_z - h_x \sin(\alpha_{in}) \\ (1 - \cos(\alpha_{in}))h_x h_z - h_y \sin(\alpha_{in}) & (1 - \cos(\alpha_{in}))h_y h_z + h_x \sin(\alpha_{in}) & (1 - \cos(\alpha_{in}))h_z^2 + \cos(\alpha_{in}) \end{bmatrix}. \tag{88}$$

Then, a proper integration method must be chosen in order to integrate Equations (86). In Section V, a fourth-order Runge Kutta method has been employed where the state vector $\vec{y}(t + \Delta t)$ at the time $t + \Delta t$ can be obtained from the previous value of vector $\vec{y}(t)$ at time t using the following equations [47],

$$\vec{y}(t + \Delta t) = \vec{y}(t) + \frac{1}{6}(\vec{k}_1 + \vec{k}_2 + \vec{k}_3 + \vec{k}_4), \tag{89}$$

$$\vec{k}_1 = \Delta t \cdot F(t, \vec{y}(t)), \tag{90}$$

$$\vec{k}_2 = \Delta t \cdot F(t + \frac{\Delta t}{2}, \vec{y}(t) + \frac{1}{2}\vec{k}_1), \tag{91}$$

$$\vec{k}_3 = \Delta t \cdot F(t + \frac{\Delta t}{2}, \vec{y}(t) + \frac{1}{2}\vec{k}_2), \tag{92}$$

$$\vec{k}_4 = \Delta t \cdot F(t + \Delta t, \vec{y}(t) + \vec{k}_3), \tag{93}$$

Acknowledgments

University of Strathclyde, United Kingdom).

References

[1]Kessler, D. J., Johnson, N. L., and Liou, J. C., Matney, M., *The kessler syndrome: implications to future space operations*, 33rd Annual AAS Guidance and Control Conference, number AAS 10-016, Breckenridge, CO, Feb. 6-10, 2010.

[2]NASA, *Orbital Debris Quarterly News*, NASA Orbital Debris Program Office, vol. 19, issue 2, April 2015.

[3]SpaceNews, *SpaceNews Website*, URL:http://spacenews.com/, date of retrieval 15-02-2016.

[4]European Space Agency, *Position Paper on Space Debris Mitigation. Implementing Zero Debris Creation Zones.*, number SP-1301, The Netherlands, Oct. 2005.

[5]National Aeronautics and Space Administration, *Process for Limiting Orbital Debris.*, number NASA-STD-8719.14A, Washington DC, Dec. 2011.

[6]Committee on the Peaceful Uses of Outer Space, United Nations Office for Outer Space Affairs, *Active Debris Removal - An Essential Mechanism for Ensuring the Safety and Sustainability of Outer Space.*, number A/AC.105/C.1/2012/CRP.16, Vienna, Feb. 2012.

[7]Bonnal, Christophe, Ruault, Jean-Marc, Desjean, Marie-Christine, *Active Debris Removal: Current Status of activities in CNES*, International Astronautical Congress, number IAC-12,A6,7,1,x16181, Naples, Italy, 2012.

[8]Castronuovo, Marco M, *Active space debris removal - A preliminary mission analysis and design*, doi:10.1016/j.actaastro.2011.04.017, Acta Astronautica, vol. 69, pp. 848-859, 2011.

[9]Lampariello, R., *On Grasping a Tumbling Debris Object with a Free-Flying Robot*, doi:10.3182/20130902-5-DE-2040.00118, 19th IFAC Symposium on Automatic Control in Aerospace Source, vol. 46, issue 19, pp. 161-166, 2013.

[10]Karavaev,Y., Kopyatkevich, R., Mishina, M., *Astrophotometrical Observation of Artificial Satellites and Study of the Technical Status of Parental Bodies of Space Debris at Geostationary Ring*, 4th European Conference on Space Debris Darmstadt, Germany, April 2005.

[11]Papushev, P., Karavaev, Y., Mishina, M., *Investigations of the evolution of optical characteristics and dynamics of proper rotation of uncontrolled geostationary articial satellites*, doi:10.1016/j.asr.2009.02.007, Advances in Space Research, vol. 43, issue 9, pp. 1416-1422, May 2009.

[12]Kawamoto, S., Matsumoto, K., Wakabayashi, S., *Ground Experiment of Mechanical Impulse Method for Uncontrollable Satellite Capturing*, 6th International Symposium on Artificial Intelligence and Robotics and Automation in Space, Canada, June 2001.

[13]Nishida, S., Kawamoto, S., *Strategy for capturing of a tumbling space debris*, doi:10.1016/j.actaastro.2010.06.045, Acta Astronautica, vol. 68, issue 1-2, pp. 113-120, Feb. 2011.

[14]McKnight, D., Pentino, F., Kaczmarek, A., Knowles, S., *Detumbling rocket bodies in preparation for active debris removal*, 6th European Conference on Space Debris, European Space Operations Centre, Darmstadt, Germany, 2013.

[15]Caubet, A., Biggs, J. D. , *Design of an Attitude Stabilization Electromagnetic Module for Detumbling Uncooperative Targets*, doi: 10.1109/AERO.2014.6836325, IEEE Aerospace Conference, Big Sky, USA, 2014.

[16]Brun, P. , *GNC Challenges for heavy active debris removal using blow effect to proces or de-tumble debris*, 5th International Conference on Spacecraft Formation Flying Missions and Technologies, 2013.

[17]Bennet, T., Schaub, H., *Touchless Electrostatic Three-Dimensional Detumbling of Large GEO Debris*, number AAS 14-378, AAS/AIAA Space Flight Mechanics Meeting, New Mexico, 2014.

[18]King, L. B., Parker, G., Deshmukh, S., Chong, J., *Study of Inter-Spacecrft Coulomb Forces and Implications for Formation Flying*, doi: 10.2514/2.6133, Journal of Propulsion and Power, vol. 19, issue 3, pp. 497-505, May 2003.

[19]Kumar, K., Ortiz Gómez, N., Jankovic, M., Romero Martín, J.M., Topputo, F., Walker S.J., Kirchner, F., Vasile, M., *Agora: Mission to demonstrate technologies to actively remove Ariane rocket bodies.*, International Astronautical Congress, number IAC-15,A6,6,1,x28851, Jerusalem, Oct. 2015.

[20]Kadaba, P. K., Naishadham, K., *Feasibility of Noncontacting Electromagnetic Despinning of a Satellite by Inducing Eddy Currents in Its Skin-Part I: Analytical Considerations*, doi: 10.1109/20.390159, Journal of IEEE Transactions on Magnetics, vol. 31, issue 4, July 1995.

[21]Sugai, F., Abiko, S., Tsujita, T., Jiang, X., Uchiyama, M., *Development of an Eddy Current Brake System for Detumbling Malfunctional Satellites*, doi: 10.1109/SII.2012.6427330, IEEE/SICE International Symposium on System Integration, pp. 325-330 Japan, 2012.

[22]Ortiz Gómez, N., Walker S.J., *Eddy Currents applied to De-tumbling of Space Debris: Analysis and Validation of Approximate Proposed Methods*, doi:10.1016/j.actaastro.2015.04.012, Acta Astronautica, vol. 114, pp. 34-53, Sept. 2015.

[23]Kong, E., Kwon, D. W., Schweighart, S. A., Elias L.M., Sedwick, R.J., Miller D.W., *Electromagnetic Formation Flight for Multisatellite Arrays*, doi: 10.2514/1.2172, Journal of Spacecraft and Rockets, vol. 41, issue 4, pp. 659-666, July 2004.

[24]Eslinger, G., Saenz-Otero, A., *Electromagnetic formation flight control using dynamic programming*, number AAS 13-012, Proceedings of Advances in the Astronautical Sciences, Guidance and Control, Colorado, USA, Feb. 2013.

[25]Reinhardt, B., Hencey, B., Peck, M. *Characterization of Eddy Currents for Space Actuation*, number AIAA 2012-4868, AIAA/AAS Astrodynamics Specialist Conference, Minnesota, USA, Aug. 2012.

[26]Fortescue, P., *Spacecraft systems engineering*, pp. 256-262, Springer, 2015.

[27]Zemoura, M., Hanada, T., Kawamoto, S., *Evaluation of the impacts of near Earth orbit debris removal and track of events' origins.*, 3rd European Workshop on Space Debris Modelling and Remediation, CNES, June, 2014.

[28]Kwon, D. W., Sedwick, R.J., Miller D.W., *Method of both cooling and maintaining the uniform temperature of an extended object*, US Patent 20120036870 A1, Massachusetts Institute of Technology, Feb. 2012.

[29]Ortiz Gómez, N., Walker S.J., *Earth's Gravity Gradient and Eddy Currents Effects on the Rotational Dynamics of Space Debris Objects: Envisat Case Study*, doi:10.1016/j.asr.2014.12.031, Advances in Space Research, vol. 56, issue 3, pp. 494-508 Aug. 2015.

[30]Fehse, W., *Automated Rendezvous and Docking of Spacecraft.*, chapter 6, chapter 7, appendix A, 2009th Edition, N.16 in Cambridge Aerospace Series, Cambridge University Press, New York, USA, October 2003.

[31]Tweddle, B. E., Settereld, T. P., Saenz-Otero, A., Miller, D. W., *An Open Research Facility for Vision-Based Navigation Onboard the International Space Station*, doi: 10.1002/rob.21622, Journal of Field Robotics, Oct. 2015.

[32]Opromolla, R., Fasano, G., Rufino, G., Grassi., M., *Uncooperative pose estimation with LIDAR-based system*, doi:10.1016/j.actaastro.2014.11.003, Acta Astronautica, vol. 110, pp. 287-297, May 2015.

[33]Fourie, D., Tweddle, B. E., Ulrich, S., Saenz-Otero, A., *Flight Results of Vision-Based Navigation for Autonomous Spacecraft Inspection of Unknown Objects*, doi: 10.2514/1.A32813, Journal of spacecraft and rockets, vol. 51, issue 6, pp. 2016-2026, Nov. 2014.

[34]Ruel, S., Luu, T., Berube., A., *Space Shuttle Testing of the TriDAR 3D Rendezvous and Docking Sensor*, doi: 10.1002/rob.20420, Journal of Field Robotics, vol. 29, issue 4, pp. 535-553, July 2012.

[35]Christian, J. A., Cryan, S., *A Survey of LIDAR Technology and its Use in Spacecraft Relative Navigation*, number AIAA 2013-4641, Proceedings of the AIAA Guidance, Navigation, and Control Conference, Honolulu, HI, USA, Aug. 2008.

[36]Lim, T. W., *Point cloud modeling using the homogeneous transformation for non-cooperative pose estimation.*, doi:10.1016/j.actaastro.2015.02.002, Acta Astronautica, vol. 111, pp. 61-67, July 2015.

[37]Nazari, M., Butcher, E., Schaub, H. *Spacecraft Attitude Stabilization using Nonlinear Delayed Multi-Actuator Control and Inverse Dynamics*, doi: 10.2514/1.58249, Journal of Guidance, Control, and Dynamics, vol. 36, issue 5, pp. 1440-1452, Sept. 2013.

[38]Sidi, M., *Spacecraft Dynamics and Control*, pp. 245, 284 and 387, Cambridge university Press, 1997.

[39]Wertz, J. R. *Spacecraft Attitude Determination and Control*, pp. 272, Dordrecht, The Netherlands, Kluwer, 1978.

[40]Chunodkar, A., Akella, M. *Attitude Stabilization with Unknown Bounded Delay in Feedback Control Implementation*, doi: 10.2514/1.50352, Journal of Guidance, Control and Dynamics, vol. 34, issue 2, pp. 535-542, March 2011.

[41]Ormsby, J. F. A., *Eddy Current Torques and Motion Decay on Rotating Shells.*, Project 8051, United States Air Force, Nov. 1967.

[42]Vanderlinde, J., *Classical Electromagnetic Theory.*, pp. 39 and 44, Second Edition, Kluwer Academic Publishers, 2004.

[43]Boyer, H. T., *The Force on a Magnetic Dipole*, doi: 10.1119/1.15501, American Journal of Physics, vol. 56, issue 8, pp. 688-692, 1988.

[44]Hughes, P. C., *Spacecraft Attitude Dynamics.*, pp. 59, Dover Publications, INC., 2004.

[45]Stengel, R., *Optimal control and estimation.*, pp.132-137, New York, Dover Publications 1994.

[46]Oppenheim, A.V. and Willsky, A.S. and Nawab, S. H. *Signals and Systems (2nd Edition).*, pp. 832-835, Prentice-Hall, Inc. Upper Saddle River, NJ, USA 1996.

[47]Douglas Faires, J., Burden, R. *Numerical methods. 3rd Edition*, Chapter 5, Thomson, 2004.

[48]Arianespace S.A., *Ariane 4 user's manual.*, issue 2, Feb. 1999.

[49]Koppenwallner, G., Fritsche, B., Lips, T., Klinkrad, H., *SCARAB - A multi-disciplinary code for destruction analysis of spacecraft during re-entry*, 5th European Symposium on Aerothermodynamics for Space Vehicles, Germany, Nov. 2004.

[50]Stardust Programme, *Advanced Research Network on Asteroid and Space Debris Manipulation*, European Union Framework Program FP7, Marie Curie Initial Training Networks (ITN), URL: http://www.stardust2013.eu/, date of retrieval 01-02-2016.,